

EXTRACTION OF WIND SPEED FROM HIGH FREQUENCY  
GROUND WAVE RADAR OCEANIC BACKSCATTER

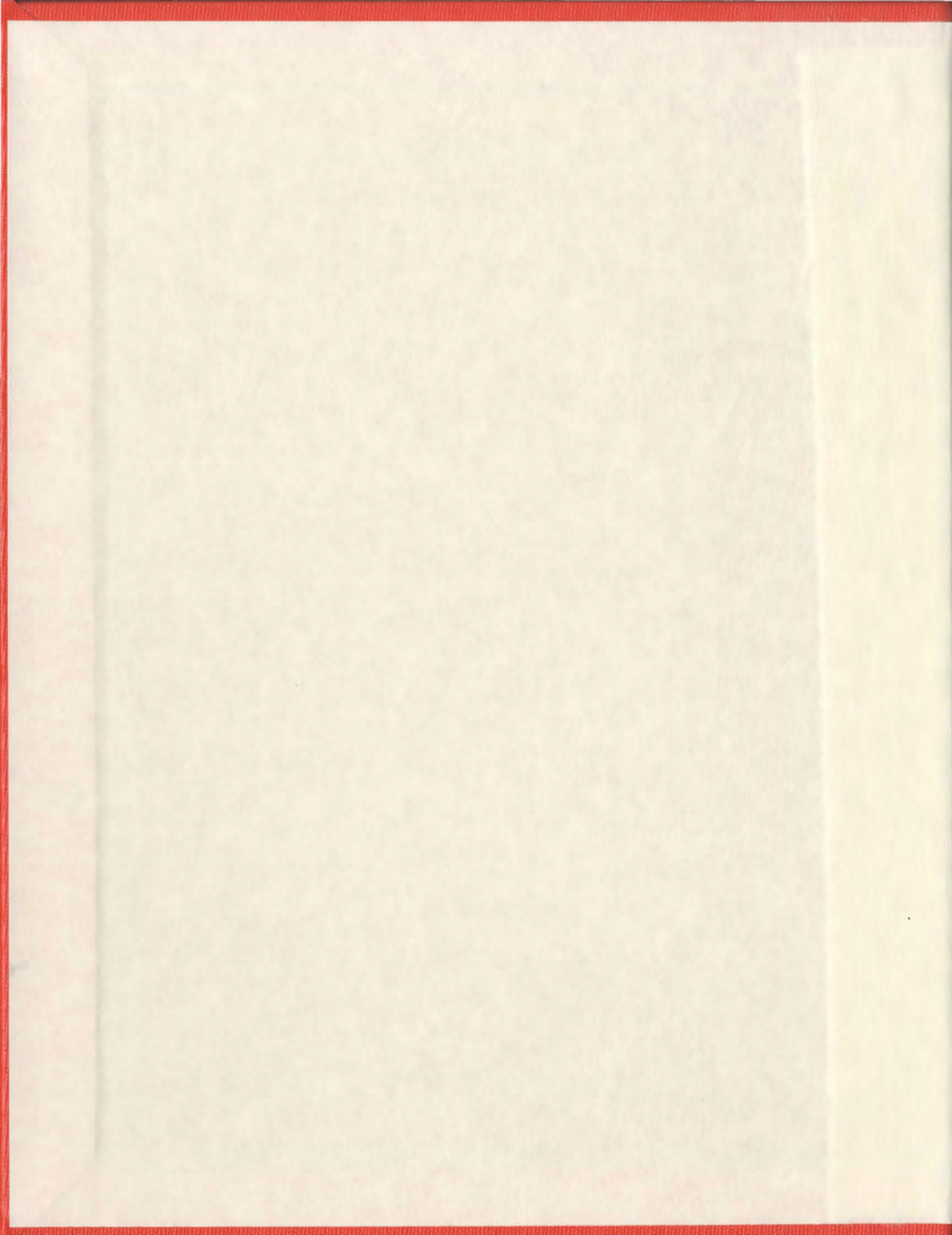
CENTRE FOR NEWFOUNDLAND STUDIES

---

**TOTAL OF 10 PAGES ONLY  
MAY BE XEROXED**

*(Without Author's Permission)*

DAVID W. GREEN



REDUCTION OF WIND EFFECTS FROM HIGH FREQUENCY URBAN WAVE  
RADAR AND RAINFALL

BY  
DAVID W. CROSS

A thesis submitted to the  
School of Graduate Studies  
in partial fulfillment of the  
requirements for the degree of  
Master of Engineering

FACULTY OF ENGINEERING AND APPLIED SCIENCE

MEMORIAL UNIVERSITY OF NEWFOUNDLAND



100-1000

Newfoundland

EXTRACTION OF WIND SPEED FROM HIGH FREQUENCY GROUND WAVE  
RADAR OCEANIC BACKSCATTER

BY

© DAVID W. GREEN

A thesis submitted to the  
School of Graduate Studies  
in partial fulfillment of the  
requirements for the degree of  
Master of Engineering

FACULTY OF ENGINEERING AND APPLIED SCIENCE

MEMORIAL UNIVERSITY OF NEWFOUNDLAND

July 2005

St. John's



Newfoundland

# Abstract

The ability to remotely sense ocean winds has numerous research and commercial applications. High Frequency radar operating in ground wave mode has proven itself to be an effective means of remotely sensing the ocean surface. This is because at the typical operating frequencies (3-30 MHz), the radar signal can travel very large distances. Also, wavelengths in this band interact closely with the most energetic ocean waves. The problem that is dealt with in this thesis is the extraction of the wind speed blowing over a radar-illuminated patch of ocean.

The Doppler spectra of the returned radar signal contain a wealth of oceanographic information. This is owing to the various complex electromagnetic scattering mechanisms. The radar cross section of the ocean surface that results has many salient features that can be used to extract particular ocean parameters. Based on the existing HF radar theory, an expression is derived that extracts the peak frequency of the ocean spectrum from the radar cross section. This spectral peak frequency is then linked to oceanographic models which dictate the growth of an ocean spectrum to a given wind condition.

The models are applied to simulated noisy data. In addition, appropriate signal processing techniques are applied to mitigate the effects of noise and to improve the robustness of the models. Finally, the models are applied to sample HF radar data provided by Rutgers University. This data was obtained from a Coastal Ocean Dynamics Applications Radar (CODAR) operating in Breezy Point, NY. The results are

then compared to ground truth data provided by the National Oceanic and Atmospheric Administration (NOAA) from a weather station located in the vicinity of the illuminated patch of ocean.

# Acknowledgments

The author would like to thank the Faculty of Engineering and Applied Science for the opportunity to conduct this body of research. In particular, the supervision of Dr. Eric Gill has proved extremely valuable during the course of this research. He provided a very interesting research topic and initial insight as to how to proceed. High frequency radar data provided by the Coastal Ocean Observation Lab at Rutgers University is also greatly appreciated.

The author is grateful for financial support in the forms of (1) graduate assistance provided by the Faculty of Engineering and Applied Science, (2) a post graduate scholarship from the Natural Sciences and Engineering Research Council (NSERC), (3) graduate support from an NSERC grant awarded to supervisor Dr. Eric Gill during the fast-track portion of the programme, and (4) a Maritime Studies Scholarship from Maritime Awards Society of Canada (MASC).

The author would also like to thank examiners Dr. Glyn George and Dr. John Walsh for their suggestions and comments. This feedback has undoubtedly contributed to the improvement of this thesis from its original version.

# Contents

<b>Abstract</b>	<b>i</b>
<b>Acknowledgments</b>	<b>iii</b>
<b>Table of Contents</b>	<b>iv</b>
<b>List of Figures</b>	<b>vi</b>
<b>List of Symbols</b>	<b>viii</b>
<b>1 Introduction</b>	<b>1</b>
1.1 Research Rationale . . . . .	1
1.1.1 Conventional Ocean Wind Speed Measurement . . . . .	2
1.1.2 HF Radar Wind Speed Measurement . . . . .	3
1.2 Literature Review . . . . .	4
1.3 Scope of Thesis . . . . .	8
<b>2 Relevant Models</b>	<b>9</b>
2.1 Ocean Spectrum Models . . . . .	9
2.2 First Order Cross Section . . . . .	14
2.3 Second Order Cross Section . . . . .	16
2.4 Noise Model . . . . .	20

<b>3</b>	<b>Recovering Wind Information</b>	<b>22</b>
3.1	Wind Direction . . . . .	22
3.2	Wind Speed . . . . .	23
3.3	Differentiating the Second Order Cross Section . . . . .	26
<b>4</b>	<b>Spectral Growth</b>	<b>36</b>
4.1	Description of spectral growth . . . . .	37
4.2	Numerical spectrum growth techniques . . . . .	42
<b>5</b>	<b>Tests on Simulated Noisy Data</b>	<b>46</b>
5.1	Extracting Simulated Wind Speed . . . . .	46
5.2	Extracting Wind Speed from Spectral Growth . . . . .	53
<b>6</b>	<b>Application of Models</b>	<b>59</b>
<b>7</b>	<b>Conclusions and Recommendations</b>	<b>68</b>
7.1	Suggestions for Further Work . . . . .	69
	<b>Bibliography</b>	<b>71</b>

# List of Figures

1.1	Typical radar cross section for operating frequency of 15 MHz, wind speed of 15 m/s and wind direction of 30° . . . . .	4
2.1	Pierson-Moskowitz spectrum at different wind speeds. . . . .	11
2.2	Comparison of JONSWAP and Pierson-Moskowitz spectra for a wind speed of 10 m/s. . . . .	13
2.3	First order cross section. . . . .	15
2.4	Second order cross section geometry . . . . .	16
2.5	Contours of constant Doppler for $m_1 = m_2$ . . . . .	18
3.1	Second order cross section for different wind speeds. . . . .	24
3.2	Contours of constant Doppler. . . . .	27
3.3	$K_1$ versus $\theta_{K_1}$ for different Doppler frequencies. . . . .	30
3.4	Wind speed as a function of second order Doppler peak. . . . .	34
4.1	JONSWAP and SPM growth curves. . . . .	40
4.2	JONSWAP growth curves for different wind speeds. . . . .	41
4.3	Growth curves for JONSWAP and numerical spectrum from energy balance equation. . . . .	45
5.1	Typical simulated noisy radar Doppler spectrum. . . . .	47
5.2	Ten averaged Doppler spectra. . . . .	48
5.3	Twenty-five averaged Doppler spectra. . . . .	49
5.4	Result of a 5-point Hamming window applied to Figure 5.3. . . . .	50
5.5	Result of a 9-point Hamming window applied to Figure 5.3. . . . .	51

5.6	Result of a 13-point Hamming window applied to Figure 5.3. . . . .	52
5.7	Wind speed recovered from conditioned Doppler spectra. . . . .	53
5.8	Ocean spectral growth for a wind speed of 10 m/s increasing to 15 m/s. . . . .	55
5.9	Noisy version of Figure 5.8. . . . .	56
5.10	Recovered wind speed from noisy $f_p(n)$ time series. . . . .	57
6.1	Sample cross section from Breezy Point run. . . . .	60
6.2	Hamming windowed cross section. . . . .	61
6.3	Radar-inferred saturated wind speeds. . . . .	63
6.4	Radar-inferred spectral peaks. . . . .	64
6.5	Radar recovered and NOAA measured wind speeds. . . . .	65
6.6	Error in radar-inferred wind speed values. . . . .	66
6.7	Radar recovered values using techniques in Section 4.2. . . . .	67

## List of Symbols

$\omega_d$	Angular Doppler frequency (p. 9)
$\sigma$	Total radar cross section (p. 9)
$\sigma_1$	First order radar cross section (p. 9)
$\sigma_2$	Second order radar cross section (p. 9)
$f$	Frequency of ocean wave (p. 10)
$\theta$	Direction of ocean wave (p. 10)
$S(f, \theta)$	Ocean wave directional spectrum (p. 10)
$F(f)$	Frequency dependent portion of the ocean spectrum (p. 10)
$G(\theta)$	Directional factor of the ocean spectrum (p. 10)
$\Gamma$	Directional spectrum proportionality constant (p. 10)
$s$	Spread parameter (p. 10)
$\theta_K$	Wave direction (p. 10)
$\theta_U$	Wind direction (p. 10)
$\alpha_{PM}$	Pierson-Moskowitz spectrum constant (p. 10)
$g$	Gravitational acceleration (p. 10)
$U_z$	Wind speed at $z$ metres above sea level (p. 10)
$\alpha_J$	JONSWAP spectrum constant (p. 12)
$a$	JONSWAP shape exponent (p. 12)
$\alpha_J$	JONSWAP coefficient (p. 12)
$X$	Fetch length (p. 12)
$\gamma$	JONSWAP shape parameter (p. 12)

$u_*$	Friction velocity (p. 12)
$z_0$	Roughness length (p. 12)
$\kappa$	von Kármán constant (p. 12)
$z$	Height above sea level (p. 12)
$\alpha_{ch}$	Charnock constant (p. 12)
$\vec{K}$	Ocean wave vector (p. 14)
$k_0$	Radar wave number (p. 14)
$\omega$	Angular frequency of ocean wave (p. 14)
$\omega_d$	Angular Doppler frequency (p. 14)
$\sigma_{11}$	First order radar cross section (p. 14)
$\Delta\rho_s$	Patch width (p. 14)
$\text{Sa}(\cdot)$	Sampling function (p. 14)
$K$	Magnitude of ocean wave vector $\vec{K}$ (p. 14)
$S_{11}(m\vec{K})$	Ocean spectrum for wave $K$ (p. 14)
$\omega_B$	Angular Bragg frequency (p. 15)
$\theta_{K_1}$	Direction of wave vector $\vec{K}_1$ (p. 16)
$\vec{K}_1, \vec{K}_2$	Constituent wave vectors of second order scatter (p. 16)
$\sigma_{2P}(\cdot)$	Second order double patch scatter cross section of ocean surface (p. 16)
$\delta(\cdot)$	Delta-Dirac function (p. 16)
$K_{1x}, K_{1y}$	Cartesian components of wave vector $\vec{K}_1$ (p. 17)
$\Gamma_T$	Hydrodynamic and electromagnetic coupling coefficient (p. 18)
$\Gamma_H$	Hydrodynamic coupling coefficient (p. 18)
$K_1, K_2$	Magnitudes of wave vectors $\vec{K}_1, \vec{K}_2$ (p. 18)
$\omega_1, \omega_2$	Angular frequencies of waves $\vec{K}_1, \vec{K}_2$ (p. 18)
$Y$	$\sqrt{K_1}$ (p. 18)

$D_p$	Delta constraint simplification function ( $-m_1\sqrt{gK_1} - m_2\sqrt{gK_2}$ ) (p. 19)
$P_c$	Average power spectral density of ocean clutter (p. 20)
$\lambda_0$	Radar operating wavelength (p. 20)
$P_t$	Average transmitter power (p. 20)
$G_t$	Transmitter gain (p. 20)
$G_r$	Receiver gain (p. 20)
$F(\rho, \omega_0)$	Spherical earth attenuation function (p. 20)
$\rho$	Range of scattering patch from radar (p. 20)
$A_e$	Effective receiving cross sectional area (p. 20)
$d_c$	Duty cycle of transmitted pulse (p. 20)
$S_N$	Noise power spectral density (p. 20)
$k$	Boltzmann's constant (p. 20)
$T_0$	Reference noise temperature (p. 20)
$F_{am}$	Noise figure (p. 20)
$P_N$	Average noise spectral density (p. 21)
$t$	Time (p. 21)
$\epsilon$	Uniformly distributed random phase term (p. 21)
$p$	Maximum discrete frequency index (p. 21)
$\omega_B^-$	Negative Bragg peak (p. 22)
$\omega_B^+$	Positive Bragg peak (p. 22)
$\theta_w$	Wind direction (p. 25)
$f_B$	Bragg frequency (p. 29)
$\beta$	Jacobian of the transformation (p. 29)
$\psi'$	$\frac{gK + (\omega_1 + \omega_2)^2}{gK - (\omega_1 + \omega_2)^2}$ (p. 29)
$A$	$K_1 + K_2 + B$ (p. 31)
$B$	$m_1 m_2 \sqrt{K_1 K_2} \psi'$ (p. 31)
$\theta_{K_2}$	Direction of wave vector $\vec{K}_2$ (p. 31)

$S_n(K_n)$	Directional ocean wave spectrum for wave $\vec{K}_n$ (p. 31)
$G_n(\theta_{K_n})$	Directional factor of ocean wave spectrum for wave $\vec{K}_n$ (p. 31)
$C$	$2^7 \pi^2 k_0^4$ (p. 31)
$C'$	$CG_1G_2$ (p. 31)
$R(K_1)$	$2A^2 + B^2$ (p. 32)
$f_0$	Radar operating frequency (p. 33)
$f_p$	Spectral peak frequency (p. 36)
$E_{PM}$	Pierson Moskowitz energy (p. 37)
$\chi$	Non-dimensional fetch (p. 38)
$\varsigma$	Non-dimensional duration (p. 38)
$\nu$	Non-dimensional frequency (p. 38)
$U_A$	Adjusted wind speed (p. 39)
$C_g$	Group velocity of ocean waves (p. 42)
$S_{tot}$	Total spectral energy change (p. 42)
$S_{in}$	Energy input from atmosphere (p. 42)
$S_{ds}$	Energy dissipated from spectrum (p. 42)
$S_{nl}$	Nonlinear spectral transfer (p. 42)
$\rho_a$	Density of air (p. 43)
$\rho_w$	Density of seawater (p. 43)
$\phi$	Normally distributed random variable (p. 54)
$\mu$	Mean of normally distributed random variable (p. 54)
$\sigma_\phi$	Standard deviation of the normally distributed random variable (p. 54)
$V_1(\omega), V_2(\omega)$	Complex frequency spectra from two loop antennas (p. 59)
$V_3(\omega)$	Complex frequency spectra from monopole (p. 59)
$a_1, a_2$	Fitted constants (p. 59)
$\omega_{SOP}$	Radial Doppler frequency of second order peak (p. 62)

$n_{SOP}$	Index of second order peak (p. 62)
$n_B$	Index of Bragg line (p. 62)
$n_{zero}$	Index of effective zero-Doppler (p. 62)
$U_{sat}$	Saturated wind speed (p. 62)

# Chapter 1

## Introduction

### 1.1 Research Rationale

The ability to remotely sense ocean winds has far-reaching applications. Most important of these is ensuring human safety. Mariners can be advised of local weather conditions for particular regions of the ocean and hence make informed decisions about the safest course to chart. Knowledge of ocean winds also facilitates the tracking of drifting vessels and survivors from nautical disasters, which in turn assists search and rescue efforts.

The growing offshore oil industry also benefits from such knowledge. Winds play a significant role in the drifting of icebergs. It would be possible then to determine whether an iceberg will come into collision with a floating platform, so that evacuation or other preemptive measures may be taken. Knowledge of the local ocean winds also allows easier tracking of oil spills, leading to more effective cleanup measures.

Finally, ocean winds have obvious meteorological applications, such as offshore hurricane detection and tracking. As oceans cover the majority of the earth's surface, knowledge of local wind speeds would only aid in developing models for more accurate weather forecasting. Physical oceanographers will be able to measure ocean

winds safely and inexpensively from the shoreline. This is much easier than the existing method of deploying measurement vessels into the sometimes dangerous ocean environment.

### **1.1.1 Conventional Ocean Wind Speed Measurement**

Currently, ocean winds are measured either by an anemometer onboard a coastal surveillance ship, by permanently moored wave buoys, or via satellite means. On a ship, the anemometer measures wind the same way that it would on land. Several drawbacks come with this method. First, a ship must be fueled and manned to survey the ocean surface. This can be very costly. Secondly, ships can only provide the measurement for a particular location on the ocean and at a particular time. Finally, there is the safety consideration of the the ship and its crew which are subject to the dangerous ocean environment.

Wave buoys are also employed. Environment Canada has deployed several buoys along the nation's coastline. Buoys have the advantage of not being manned, so their operating cost is lower as is the risk of endangering human life. They also provide continuous coverage once deployed. However, they can only monitor the one point of the ocean surface they occupy. To provide more coverage would involve deploying many wave buoys which would be very expensive. Also, as they are susceptible to the harsh ocean environment. wave buoys require frequent maintainence.

Ocean winds can also be measured by satellite means, such as the SeaWinds scatterometer aboard the QuickSCAT satellite operated by the National Aeronautics and Space Administration (NASA). Microwaves emitted from the satellite are scattered by the ocean surface and the returned signal is processed to extract the ocean winds. Implementation of such as system is obviously very costly. In addition, since the satellite must orbit the Earth. it can only monitor a particular patch of ocean for a particular time.

### 1.1.2 HF Radar Wind Speed Measurement

The ocean, being both an extremely dangerous environment and vast area, would best be monitored via a remote sensing tool such as high frequency (HF) radar. An HF radar unit can operate in two modes when interrogating the ocean surface. Sky wave radar directs its beam towards the ionosphere which then reflects the electromagnetic energy towards its intended target. The returned signal, or backscatter, is reflected back to the radar via the same route. Tremendous ranges can be achieved by sky wave radar. However, the returned signal is normally highly contaminated by ionospheric interference. The composition of the ionosphere varies throughout the year, indeed throughout the day, and also responds unpredictably to astronomical events such as sunspots.

Ground, or surface, wave radar is considerably less affected by ionospheric contamination. In the HF band of frequencies (3-30 MHz), the sea surface operates as an excellent conductor. In the lower end of this band, the radar signal can travel distances of up to 450 kilometres, much greater than traditional line-of-sight radar systems. In addition, the wavelengths produced by this band range from ten metres to a hundred metres, which is the same order as the wavelengths of ocean waves. The signal will therefore interact intimately with the ocean surface and the "echo" will contain a wealth of information about the state of the sea.

The sea condition is largely a product of local wind. Waves are generated from the energy input by the wind as it blows over the ocean surface. These waves will behave in different manners depending on the strength and duration of the wind. It should therefore be possible to work backwards. Given a snapshot or series of snapshots of the sea state extracted from the returned HF radar signal, it should be possible to link these to oceanographic models in order to find the generating wind condition.

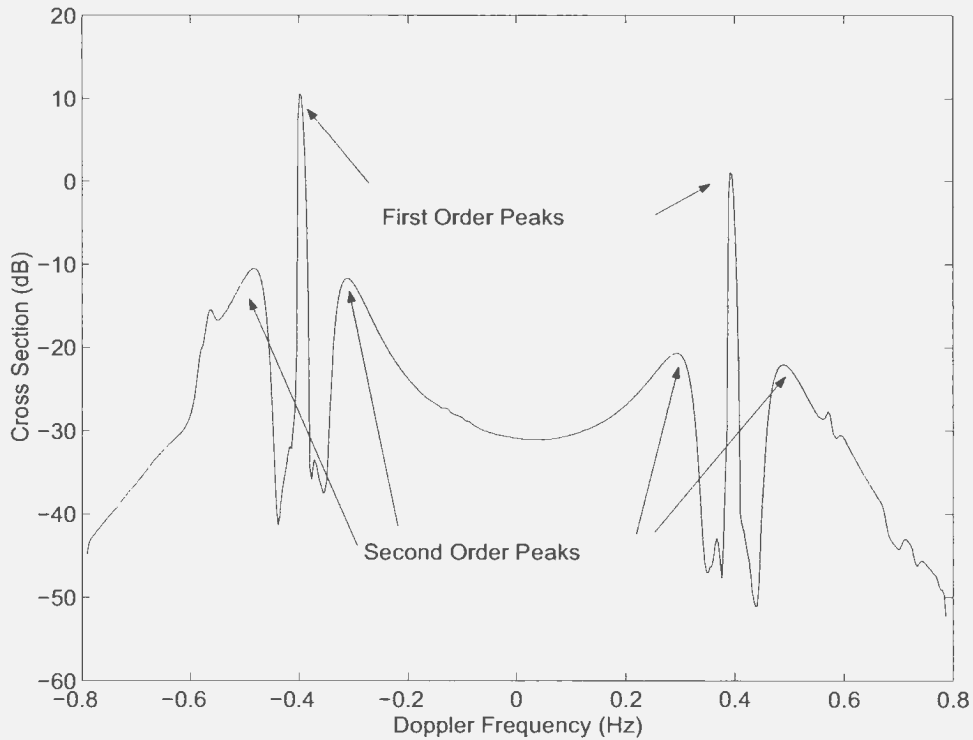


Figure 1.1: Typical radar cross section for operating frequency of 15 MHz, wind speed of 15 m/s and wind direction of  $30^\circ$ .

## 1.2 Literature Review

Crombie [1] noted that the Doppler spectrum of echo from an HF radar operating in surface wave mode over the ocean surface exhibited peaks above and below the carrier frequency. These discrete Doppler shifts are produced exclusively by waves that have a length of one-half the radar wavelength: one moving away from the radar, one moving toward the radar. He correctly deduced that Bragg scattering [2] is the physical mechanism responsible for this behaviour. The peaks resulting from the first-order Bragg scatter can be seen in Figure 1.1.

Crombie's results were later verified by Barrick and Peake [3] based on a reduction of the boundary perturbation theory of Rice [4] as applied to the analysis of backscatter from a slightly rough surface. Wait [5] also cited Bragg scatter as an explanation for the results of his analysis of backscatter from sinusoidal waves.

Barrick [6] went on to develop a theoretical model of the first order cross section that was consistent with Crombie's observations. This cross section model assumed plane-wave incidence and infinite conductivity of the scattering patch. Walsh *et al.* [7] later derived a model of the first order cross section without these assumptions. They hence produced a more realistic model with the Bragg peaks represented by sampling functions instead of delta functions.

Surrounding the Bragg peaks is a continuum of backscatter that still needed to be explained. Ward [8] first suggested that this continuum is due to higher order wave interactions. Hasselmann [9] first proposed the two sources of spectral contribution: the second order terms for scatter from Rice's boundary perturbation theory, and the second order terms from the hydrodynamic equations which describe the water surface height. Hasselmann, along with Crombie [10] and Barrick [11], also suggested that the second order backscatter could be used to recover more information about the sea state.

Barrick [12] developed a mathematical model for the second order cross section via perturbation analysis. He found that this cross section was related to the directional ocean wave spectrum via a non-linear two-dimensional Fredholm integral. Barrick's second order expression once again assumed plane-wave incidence and infinite conductivity. Gill and Walsh [13] derived an expression that, more realistically, incorporated a dipole source.

Extraction of the wind direction from the Bragg peaks of the radar return has been extensively documented [14], [15]. All methods involve an expression which relates the mean wave direction to the ratio of the left and right first-order Bragg peaks (see Figure 1.1). The only uncertainty lies in the fact that the wave directional models used in the derivation are strongly dependent on wind speed, and hence *a priori* knowledge of the wind speed is required for accurate results [16]. Heron and Rose [17], however, made the case that the ocean waves represented by the Bragg

peaks are shorter and will tend to respond very quickly to changes in the local wind conditions.

Stewart and Barnam [14] postulated that the 10 dB width of the first order Bragg peak could be used to estimate the local wind speed. However, the use of this parameter was found not to be robust, as it requires a specific spectral resolution and is dependent on factors other than wind speed [18].

It has been noted extensively in the literature (e.g., Barrick [12] and Gill [19]) that the second order return is greatly dependent on the local wind speed. The peaks of the second order return both increase in amplitude and move closer to the first order Bragg peaks with higher wind speeds. Barrick [20] originally suggested using the ratio of the second order peak amplitudes to the Bragg peak amplitude in order to find the local wind conditions.

Ahearn *et al.* [21] first proposed using the ratio of the second order continuum closer to zero Doppler to the amplitude of the first order Bragg peak for wind speed extraction. The short waves represented by the continuum in this region will more likely reflect the local wind conditions since they are the first to be excited by the wind. This method was extended upon by Gaffard and Parent [22] who introduced a correction factor to account for the dependence of this ratio on the radar beam direction relative to the wind direction. The results of their study were quite encouraging. However, the scatter between observed and radar-inferred values of wind speed was still quite high.

Dexter and Theodorides [16] outline two methods that estimate wind speed using significant wave height and period. One method employs the Sverdrup, Munk, and Bretschneider (SMB) curves, outlined in detail by Kinsman [23]. The other method employs relationships developed by the Joint North Sea Wave Project (JONSWAP) [24]. Huang *et al.* [25] have used the SMB curves in determining the wave parameters for a region of the China Sea. The radar inferred wind speeds were in fairly good

agreement with the ship measured counterparts.

The methods referred to above are viable. However they break down for high sea states and higher frequencies due to the inadequacy of the non-linear wave theory in these situations [26]. There is also an approximation in the electromagnetic scatter theory which is violated [6]. Both methods have also been demonstrated to be subject to contamination due to the presence of swell [27]. Wyatt [28] proposed that the swell component of the measurement could be identified and then removed. It was later shown that this approach could not be taken in general since the direction of swell travel can be much different than the wind direction inferred from the first order Bragg peaks [29].

All of the HF radar literature pertaining to wind speed extraction makes very little reference to the temporal nature of the response of the ocean surface to a particular wind condition. Oceanographers have documented this behaviour, the so-called duration-limited wave growth, though not extensively. The JONSWAP project [24] details a relation that models the growth of ocean waves as a function of both time and wind speed. The Coastal Engineering Research Corps (CERC) 1977 Shore Protection Manual (SPM) [30] outlines a similar model. This was updated in the 1984 SPM to use a relationship that was more consistent with the JONSWAP model.

An ocean wave modelling project headed by the SWAMP group [31] sought to describe the evolution of the sea state as a balance of source terms. Many forms were proposed for these source terms. The most problematic is the nonlinear transfer source term, a six-dimensional Boltzmann integral whose evaluation is very computationally demanding. A parameterized form of this term, called the Discrete Interaction Approximation is presented by Hasselmann *et al.* [32]. Resio and Perrie [33] later improved on this approximation.

### 1.3 Scope of Thesis

This body of work represents a method of wind information extraction from the Doppler spectra of high frequency ocean clutter. In deriving the expression relating the spectral peak to the location of the second order peaks of the radar cross section, it is assumed that the ocean is fully developed. Later, this spectral peak is taken to represent a wind-driven sea that is currently in development, since the spectral peak is a time varying quantity for any given wind condition. It is also assumed that the ocean spectrum will not be significantly limited by fetch; that is, temporal spectral development is taken to occur regardless of the distance of the wind field from the shoreline. Finally, the analysis assumes deep-water spectral analysis, that is dekametric water depths. To the best of the author's knowledge, this technique of wind speed extraction from HF radar backscatter has not been attempted.

In Chapter 2, the mathematical models developed to date which represent the radar cross section of the ocean surface, and which include noise, are overviewed. Also in this chapter are mathematical models which represent the ocean spectrum. The derivation of an expression which relates the *saturated wind speed* to discernible features of the radar Doppler spectrum is outlined in Chapter 3. In Chapter 4, the recovered wind speed is converted to a spectral peak, and a differential equation which represents the change in the spectral peak given a wind condition and the passage of time is derived. The susceptibility of the models given in Chapter 3 and Chapter 4 to noise is addressed in Chapter 5, and measures of mitigating these effects via several signal processing methods are also discussed. The utility of all of the presented models is demonstrated in extracting information from sample data collected at Breezy Point, NY by Rutgers University, and the results are compared to ground truths provided by the National Oceanic and Atmospheric Administration (NOAA). Finally, the overall results are presented in Chapter 7 and suggestions for further work are outlined.

## Chapter 2

### Relevant Models

When the electromagnetic signal is returned from the ocean surface, it is mixed with a radio frequency (RF) signal and then converted to a periodogram which shows the response of the radar return for a particular Doppler frequency. The periodogram is frequently referred to as the *radar cross section* of the ocean surface. The cross section of the ocean surface can be roughly broken down into first and second order cross sections. Each constituent cross section is added to yield an overall cross section; i.e.

$$\sigma(\omega_d) = \sigma_1(\omega_d) + \sigma_2(\omega_d) \quad (2.1)$$

where  $\omega_d$  is the angular Doppler frequency and  $\sigma_x$  represents the different cross sections. A depiction of a typical, ideal overall radar cross section can be seen in Figure 1.1. The constituent radar cross sections will be discussed in Section 2.2 and Section 2.3. First, several ocean wave models will be discussed.

#### 2.1 Ocean Spectrum Models

The state of the ocean environment is mathematically characterised by a wind-wave ocean spectrum. An ocean spectrum provides a measure of how much energy a wave with a certain frequency and in a certain direction has in a region of ocean due to a

particular wind speed. Many mathematical models for wind wave ocean spectra exist, including the Philips spectrum, the Pierson-Moskowitz spectrum, and the JONSWAP spectrum. Typically a directional ocean spectrum has the form

$$S(f, \theta) = F(f)G(\theta) \quad (2.2)$$

where  $F(f)$  represents the prevalence of a particular ocean wave frequency  $f$  and  $G(\theta)$  is the directional factor which accounts for the azimuthal direction of travel.  $G(\theta)$  has the property that

$$\int_{-\pi}^{\pi} G(\theta)d\theta = 1 \quad (2.3)$$

and is usually of the form

$$G(\theta) = \Gamma \cos^{2s} \left( \frac{\theta_U - \theta_K}{2} \right) \quad (2.4)$$

where  $s$  is the spread parameter,  $\theta_U$  is the angle of the wind direction, and  $\theta_K$  is the angle of the wave vector.  $\Gamma$  is a proportionality constant that ensures equation (2.3) is satisfied. It has been found that  $s = 2$  for many applications [25], which leads to  $\Gamma = 4/(3\pi)$ .

The Pierson-Moskowitz spectrum for fully developed seas is still in frequent use, and mathematically defined as

$$F(f) = \frac{\alpha_{PM}g^2}{(2\pi)^4 f^5} \exp \left[ -0.74 \left( \frac{g}{2\pi U_{19.5} f} \right)^4 \right] \quad (2.5)$$

where  $\alpha_{PM} = 0.0081$  is the Pierson-Moskowitz constant, and  $U_{19.5}$  is the speed of the wave-generating wind at 19.5 m above sea level. Figure 2.1 illustrates the Pierson-Moskowitz spectrum for wind speeds of 10, 15, and 20 meters per second. A more popular ocean spectrum model is the JONSWAP (Joint North Sea Wave Project) spectrum which is tailored towards a growing wind sea. It has the same basic form

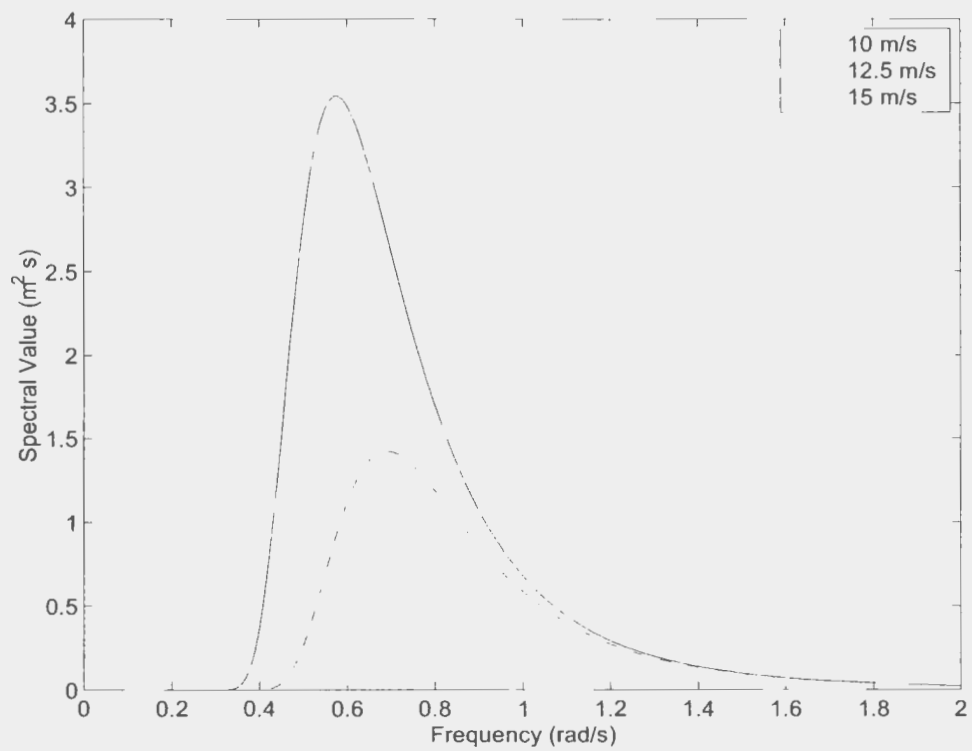


Figure 2.1: Pierson-Moskowitz spectrum at different wind speeds.

as the Pierson-Moskowitz spectrum, except that it is multiplied by a shape factor  $\gamma^a$  which accounts for fetch-limited and duration-limited spectral growth. Mathematically it is defined as

$$F(f) = \frac{\alpha_J g^2}{(2\pi)^4 f^5} \exp \left[ -0.74 \left( \frac{g}{2\pi U_{19.5} f} \right)^4 \right] \gamma^a \quad (2.6)$$

where

$$a = \exp \left[ -\frac{(f - f_p)^2}{2\sigma^2 f_p^2} \right] \quad (2.7)$$

and

$$\alpha_J = 0.076 \left( \frac{Xg}{U_{10}^2} \right)^{-0.22} \quad (2.8)$$

where  $X$  is the fetch and

$$\gamma = 3.3 \quad (2.9)$$

$$\begin{aligned} \sigma_J &= 0.07 & f < f_p \\ \sigma_J &= 0.09 & f > f_p \end{aligned} \quad (2.10)$$

The wind speed  $U_{10}$  used in the JONSWAP model is referenced at 10 m above sea level. Expressions for the fetch  $X$  will be developed in Chapter 4. A plot contrasting the JONSWAP spectrum with the Pierson-Moskowitz spectrum for a wind speed of  $U_{10} = 10$  m/s is shown in Figure 2.2. Ocean winds are frequently measured from different heights above sea level. These can be related, however, by employing the logarithmic profile of ocean winds over the sea surface. The governing equation is [23]

$$U(z) = \frac{u_*}{\kappa} \log \left( \frac{z}{z_0} \right) \quad (2.11)$$

where  $z$  is the height above sea level,  $u_*$  is the friction velocity, and  $z_0$  is the roughness length. The von Kármán constant has an accepted value of  $\kappa = 0.4$ . Further,  $u_*$  and

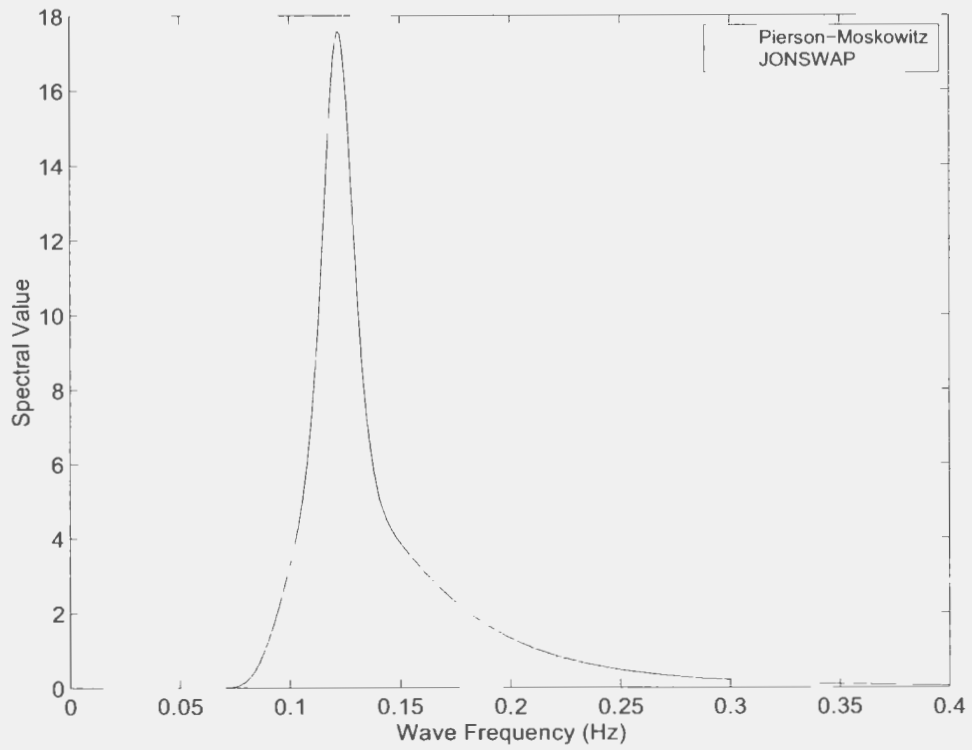


Figure 2.2: Comparison of JONSWAP and Pierson-Moskowitz spectra for a wind speed of 10 m/s.

$z_0$  are related by the Charnock relation [34]

$$z_0 = \frac{\alpha_{ch} u_*^2}{g} \quad (2.12)$$

where  $\alpha_{ch} = 0.0144$ . Hence, for a given wind speed  $U$  at a height  $z$  above the ocean surface, the parameter  $z_0$  can be found and used to extract other  $U$  values at different heights.

## 2.2 First Order Cross Section

Crombie [1] showed that the mechanism primarily responsible for the first order cross section is Bragg scattering. Electromagnetic wavelengths in the HF band are on the order of tens of metres, which closely match the lengths of waves in the most energetic part of the ocean spectrum. Therefore an EM wave of length  $\lambda$  travelling along the ocean surface will resonate over ocean waves of length  $\lambda/2$  when scattered. In terms of wave numbers the Bragg condition becomes

$$K = 2k_0 \quad (2.13)$$

where  $K = \omega^2/g$  is the ocean wave number and  $k_0$  is the radar wave number. Barrick originally modelled the Bragg scattering with Dirac Delta functions, under the assumption that the scattering patch of ocean was infinite. Walsh *et al.* [7], however, have relaxed these assumptions and modelled the first order cross section with sampling functions. Mathematically, the first order cross section is given as

$$\sigma_{11}(\omega_d) = 2^4 \pi k_0^2 \sum_{m=-1,1} \frac{K^{5/2}}{\sqrt{g}} S_{11}(m\vec{K}) \text{Sa}^2 \left[ \frac{\Delta\rho_s}{2} (K - 2k_0) \right] \quad (2.14)$$

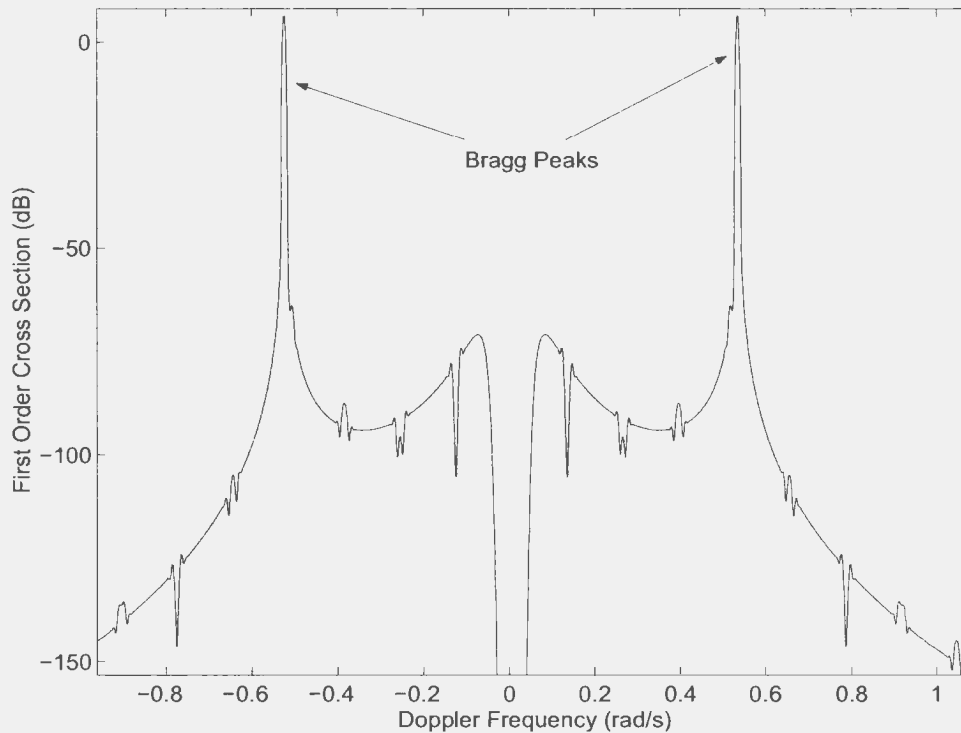


Figure 2.3: First order cross section.

where  $S_{11}(m\vec{K})$  is the ocean spectrum and  $\text{Sa}(x) = \sin(x)/x$  is the sampling function. Here the Doppler axis is broken down into two zones

$$\begin{aligned} m &= 1 & \omega_d < 0 \\ m &= -1 & \omega_d > 0 \end{aligned} \tag{2.15}$$

where the Doppler radial frequency  $\omega_d = -m\sqrt{gk}$ . From equation (2.14) it can be seen that the peaks occur when the argument of the sampling function is zero. That is,

$$\omega_d = \pm\sqrt{2gk_0} = \pm\omega_B, \tag{2.16}$$

which is the Bragg frequency for a given radar operating frequency.

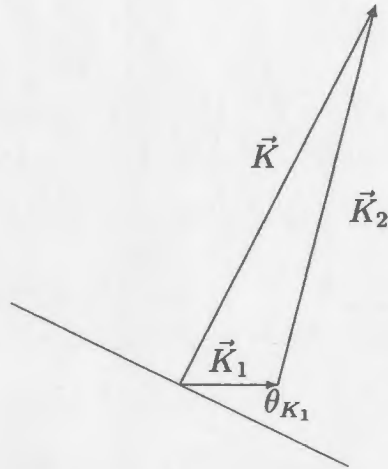


Figure 2.4: Second order cross section geometry

## 2.3 Second Order Cross Section

Second order radar return is due to the second order scatter terms from Rice's perturbation theory, and the second order hydrodynamic terms which describe the water surface. This cross section can be further broken down into three components:

1. Scatter which results from a first order scatter near the transmitter followed by a first order scatter at the illuminated patch.
2. Scatter which results from a first order scatter at the illuminated patch followed by a first order scatter near the receiver
3. Double scatter at the illuminated patch

It is the last of these three that is of most interest. The geometry for this situation is given in Figure 2.4. The wave  $\vec{K}_1$  represents the wave between the transmitter and first scatter point, and the wave  $\vec{K}_2$  represents the wave between the first and second scatter points.

The radar cross section due to this behaviour has been derived by Barrick [12] and is given by

$$\begin{aligned} \sigma_{2P}(\omega_d) \approx & 2^6 \pi^2 k_0^4 \sum_{m_1=\pm 1} \sum_{m_2=\pm 1} \int_{-\pi}^{\pi} \int_0^{\infty} S(m_1 \vec{K}_1) S(m_2 \vec{K}_2) |\Gamma_T|^2 \\ & \cdot \delta \left( \omega_d + m_1 \sqrt{gK_1} + m_2 \sqrt{gK_2} \right) K_1 dK_1 d\theta_{K_1} \end{aligned} \quad (2.17)$$

The cross section is found by integrating over all possible arrangements of  $\vec{K}_1$  and  $\vec{K}_2$  that result from varying  $\theta_{K_1}$  over the interval  $[-\pi, \pi)$ . The magnitudes  $K_1$  and  $K_2$  are limited by the delta constraint of equation (2.17):

$$\omega_d + m_1 \sqrt{gK_1} + m_2 \sqrt{gK_2} \quad (2.18)$$

Further,  $K_2$  is related to  $K_1$  by the law of cosines

$$K_2^2 = K_1^2 + K^2 - 2K_1 K \cos(\theta_K - \theta_{K_1}) \quad (2.19)$$

The parameters  $m_1$  and  $m_2$  can take on values of 1 or -1. They therefore delineate the different Doppler regions of the cross section. These regions and the corresponding values of  $m_1$  and  $m_2$  are listed below.

$$\begin{aligned} m_1 = 1 \quad m_2 = 1 \quad \omega_d < -\omega_B \\ m_1 = -1 \quad m_2 = 1 \quad -\omega_B < \omega_d < 0 \\ m_1 = 1 \quad m_2 = -1 \quad 0 < \omega_d < -\omega_B \\ m_1 = -1 \quad m_2 = -1 \quad \omega_d > \omega_B \end{aligned} \quad (2.20)$$

The vectors  $\vec{K}_1$  and  $\vec{K}_2$  trace out closed contours for different Doppler frequencies  $\omega_d$ . These contours can be seen in Figure 2.5 for  $m_1 = m_2$ . Note that for Doppler frequencies  $|\omega_d| \leq \sqrt{2}\omega_B$ , the locus surrounds only one of the two focal points. For larger

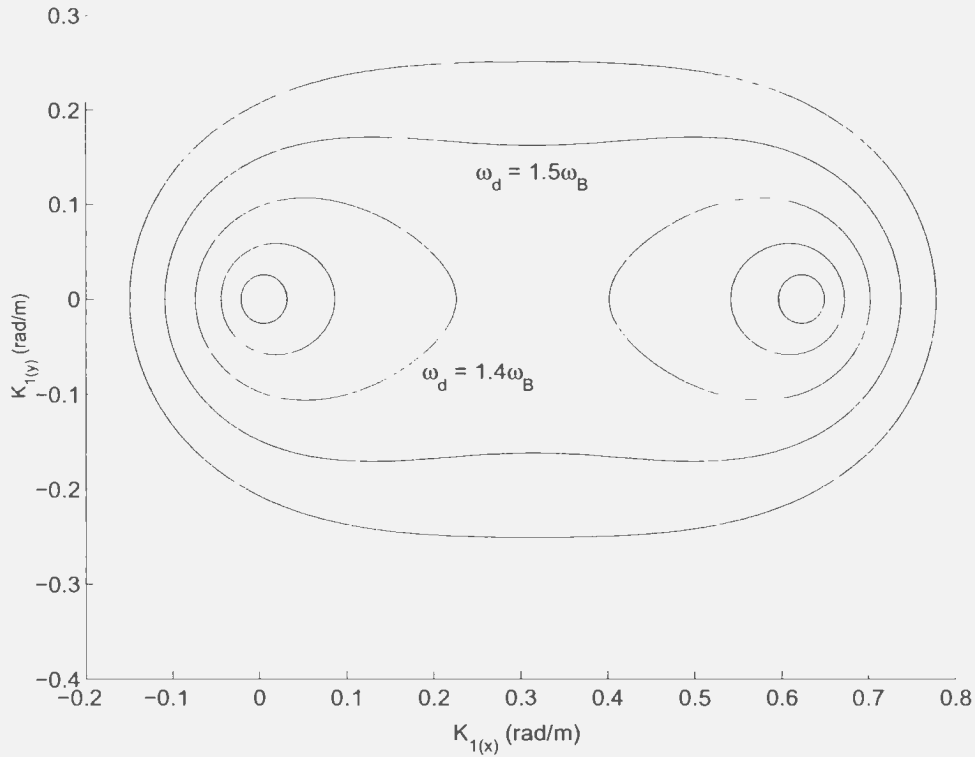


Figure 2.5: Contours of constant Doppler for  $m_1 = m_2$ .

magnitude Doppler frequencies, the locus will surround both focal points. Finally,  $\Gamma_T$  is the hydrodynamic and electromagnetic coupling coefficient. The hydrodynamic portion  $\Gamma_H$  of  $\Gamma_T$  is defined as

$$\Gamma_H = \frac{j}{2} \left( K_1 + K_2 + \frac{g}{\omega_1 \omega_2} (K_1 K_2 - \vec{K}_1 \cdot \vec{K}_2) \frac{gK + (\omega_1 + \omega_2)^2}{gK - (\omega_1 + \omega_2)^2} \right) \quad (2.21)$$

with  $\omega_n = \sqrt{gK_n}$ .

The expression in equation (2.17) can be simplified by applying the delta constraint to the inner integral. To do so, the arguments of the delta function must be expressed in terms of  $\vec{K}_1$ . Lipa and Barrick [35] approach this by first defining

$$Y = \sqrt{K_1} \quad (2.22)$$

with differentials related by

$$2YdY = dK_1 . \quad (2.23)$$

Next, the function  $D_p$  is defined as

$$D_p = -m_1\sqrt{gK_1} - m_2\sqrt{gK_2} = -m_1\sqrt{g}Y - m_2\sqrt{g}(Y^4 + K^2 - 2KY^2 \cos \theta_{K_1})^{1/4} \quad (2.24)$$

such that the delta constraint becomes  $\delta(\omega_d - D_p)$ . Finally, the differential  $dD_p$  is introduced via the Jacobian of the transformation

$$dY = \left| \frac{\partial Y}{\partial D_p} \right| dD_p \quad (2.25)$$

with

$$\left| \frac{\partial Y}{\partial D_p} \right| = \frac{1}{\sqrt{g} \left| 1 + \frac{L(Y^3 - 2Yk_0 \cos(\theta_{K_1} - \theta_K))}{[Y^4 + 4k_0^2 - 4Y^2k_0 \cos(\theta_{K_1} - \theta_K)]^{3/4}} \right|} \quad (2.26)$$

Hence the second order radar cross section can be expressed as

$$\sigma_{2P}(\omega_d) = 2^{\bar{r}} \pi^2 k_0^4 \int_{-\pi}^{\pi} \int_{D_p} S(m_1 \vec{K}_1) S(m_2 \vec{K}_2) |\Gamma_{II}|^2 \delta(\omega_d - D_p) Y^3 \left| \frac{\partial Y}{\partial D_p} \right| dD_p d\theta_{K_1} \quad (2.27)$$

For each Doppler frequency  $\omega_d$  and angle  $\theta_{K_1}$ , a value of  $Y$  is sought such that the following is satisfied

$$D_p(Y, \theta_{K_1}) - \omega_d = 0 \quad (2.28)$$

This is typically done via numerical solving methods, such as the Newton-Raphson root finding algorithm [36].

## 2.4 Noise Model

The cross sections presented in Sections 2.2 and 2.3 are idealized models. They are effectively the average of all measurements over all locations for each given condition. Also, they fail to account for external noise limiting at high frequencies. The wind parameter extraction techniques presented in Chapter 3 are highly sensitive to noise. It is necessary to quantify the effect of noise and develop theoretical signal processing techniques to limit it.

The average power spectral density of the ocean clutter  $P_c$  as returned to the receiving antenna array is given by the radar range equation

$$P_c(\omega_d) = \frac{\lambda_0^2 d_c P_t G_t G_r |F(\rho, \omega_0)|^4 A_e \sigma(\omega_d)}{(4\pi)^3 \rho^4} \quad (2.29)$$

where  $P_t$  is the average transmitter power,  $G_t$  and  $G_r$  are, respectively, the gains of the transmitting and receiving antenna array,  $A_e$  is the effective cross sectional area of the receiving array, and  $d_c$  is the duty cycle of the transmit pulse.  $F(\rho, \omega_0)$  is the spherical earth attenuation function [37] for a given patch range  $\rho$  and radar radial operating frequency  $\omega_0$ .

The power spectral density of the external noise must now be found. External noise may be categorized as atmospheric, galactic, or manmade [38]. The effects of these noise sources is dependent on the location, time, and frequency of operation. The value of the noise figures can be measured for particular operating conditions, but for the purposes of this discussion an average value will be sufficient.

It is assumed that the noise is a stationary, white, Gaussian process. Hence, the power spectral density is [38]

$$S_N(\omega) = \frac{kT_0}{2\pi} 10^{F_{am}/10} \quad (2.30)$$

in which  $k$  is Boltzman's constant ( $1.38 \times 10^{-23}$  J/K),  $T_0$  is the reference temperature (290K) and  $F_{am}$  is the noise figure. It should be noted that  $S_N(\omega) = 0$  outside of the noise bandwidth of the receiving array.

Typically a radar sends out a stream of many pulses. In this case, Gill [19] has shown that for sampling at the pulse centre, the external Doppler noise spectral density becomes

$$P_N(\omega_d) = d_c S_N(\omega) \sum_{m=\lfloor \frac{-1}{2d_c} \rfloor}^{\lceil \frac{-1}{2d_c} \rceil} \text{Sa}[m\pi d_c] \quad (2.31)$$

The power spectral densities of clutter in equation (2.29) and noise in equation (2.31) are based on an infinite time series. More realistically, a radar cross section is based on a finite time series. This can be emulated by employing Pierson's model for a single variable stationary Gaussian process [39]. For a given spectral form (either clutter or noise)  $F(\omega)$ , the finite time signal becomes

$$f(t) = \int_B e^{j\omega t} e^{j\epsilon} \sqrt{F(\omega)} d\omega \quad (2.32)$$

where  $\epsilon$  is a random phase term which has a uniform distribution over the interval  $\epsilon \in [0, 2\pi)$ . The differential under the square root precludes the possibility of an analytical expression for  $f(t)$ ; however, the integral can be approximated by the summation

$$f(t) = \sum_{k=0}^P e^{j\omega_k t} e^{j\epsilon} \sqrt{F(\omega_k) \Delta\omega} . \quad (2.33)$$

As in [19], the time series of both the ocean clutter and the external noise are calculated and then added to get a representation of the total returned signal. The signal is then converted back into the frequency domain via Fourier transformation to yield a simulated noisy cross section.

# Chapter 3

## Recovering Wind Information

### 3.1 Wind Direction

The Bragg peaks of the first order cross section can be used to obtain the wind direction. The derivation, originally done by Stewart and Barnum [14] is straightforward. The value of the first order cross section at the negative Bragg peak ( $\omega_B^-$ ) is given by substituting  $m = 1$  and  $K = 2k_0$  into equation (2.14). The sampling function reduces to unity, giving

$$\sigma_1(\omega_B^-) = 2\pi^4 k_0^2 \frac{K^{5/2}}{\sqrt{g}} \left[ \frac{\alpha_{PM}}{4K^4} \exp\left(\frac{-0.74g^2}{K^2U^4}\right) \right] \left[ \frac{4}{3\pi} \cos^{2s}\left(\frac{\theta_K - \theta_U}{2}\right) \right]. \quad (3.1)$$

Similarly, the positive Bragg peak ( $\omega_B^+$ ) is given by substituting  $m = -1$  and  $K = 2k_0$  into equation (2.14):

$$\sigma_1(\omega_B^+) = 2\pi^4 k_0^2 \frac{K^{5/2}}{\sqrt{g}} \left[ \frac{\alpha_{PM}}{4K^4} \exp\left(\frac{-0.74g^2}{K^2U^4}\right) \right] \left[ \frac{4}{3\pi} \cos^{2s}\left(\frac{\pi + \theta_K - \theta_U}{2}\right) \right] \quad (3.2)$$

Only the directional factors differ in these two equations. Making use of the identity  $\cos(x + \pi/2) = -\sin(x)$ , and dividing equation (3.2) by equation (3.1) gives

$$\frac{\sigma_1(\omega_B^+)}{\sigma_1(\omega_B^-)} = \tan^{2s}\left(\frac{\theta_U - \theta_K}{2}\right) \quad (3.3)$$

which is easily solved for  $\theta_U$  to obtain

$$\theta_U = \theta_K + 2 \tan^{-1} \left( \left( \frac{\sigma_1(\omega_B^+)}{\sigma_1(\omega_B^-)} \right)^{1/2s} \right) \quad (3.4)$$

For monostatic operation, this wind direction is ambiguous. That is, it cannot be determined whether the wind is blowing from the left or the right of the radar beam. Usually this ambiguity can be resolved by additional meteorological information. For example, winds blow in a counterclockwise fashion around a low pressure system in the Northern hemisphere. Huang *et al.* [25] have recently developed another method for resolving this ambiguity, involving minimizing the sum of differences from three readings representing three different angles.

This method of wind direction extraction assumes that the Bragg waves ( $\omega = \omega_B$ ) are travelling in the same direction as the wind. Ocean waves respond to a given wind condition with different time scale responses according to their length. Heron *et al* [17] have concluded that the waves represented by the Bragg peaks are relatively short and will therefore respond very quickly to the local wind conditions. The time response is typically under ten minutes, and hence it is reasonable to assume that the wind direction extracted via this method is accurate.

## 3.2 Wind Speed

As noted in Section 2.3, the second order radar cross section exhibits peaks surrounding the Bragg peaks of the first order cross section. These second order peaks are highly dependent upon the wind speed. Also, they can be clearly distinguished from the first order cross section, as they are typically 10 to 20 dB higher than the first order cross section. Figure 3.1 shows the second order cross section for wind speeds of 10 m/s, 15 m/s, and 20 m/s. As can be seen, the peaks grow and become more prominent at a higher wind speed. Also, the position of the peaks on the Doppler axis

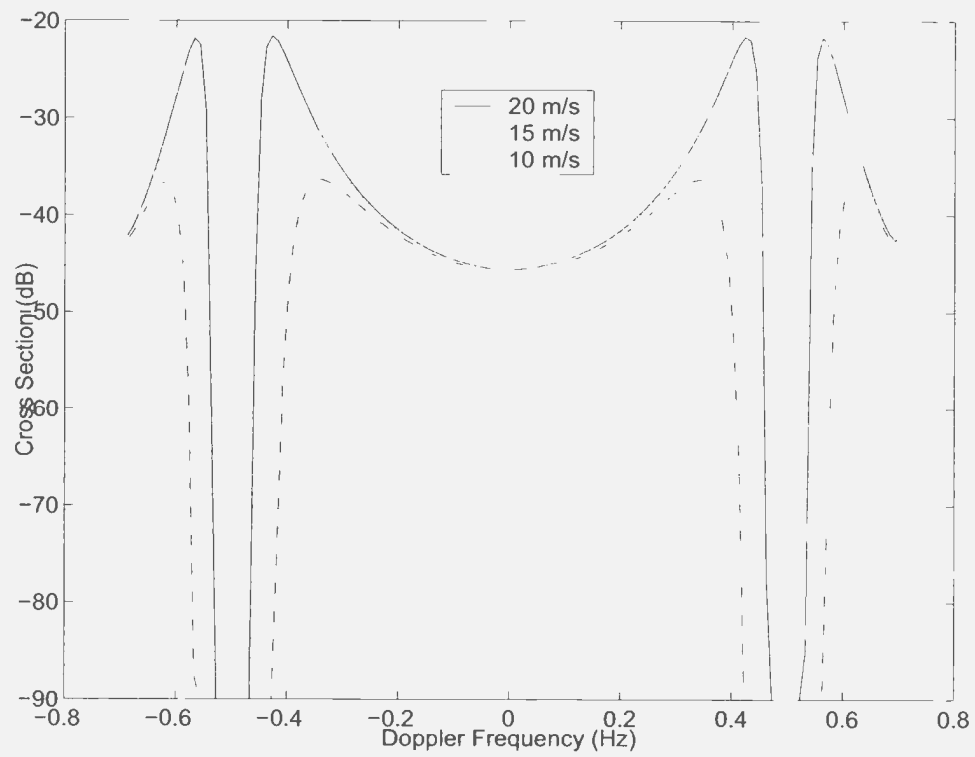


Figure 3.1: Second order cross section for different wind speeds.

changes: for higher wind speeds, the peaks are located closer to the Bragg frequency. From this it should be possible to relate both the power of the peak as well as the position of the peak to the wind speed.

### **Relating by Power**

The power of the second order peaks depend on many factors other than the wind speed:

1. Ocean spread parameter ( $s$ )
2. Wind direction ( $\theta_w$ )
3. Range of the illuminated patch from the radar
4. Operating frequency

Hence relating by power requires *a priori* knowledge of all of these parameters before the wind speed can be inferred. The operating frequency and range are often known, but determining the spread parameter can be very difficult. The wind direction can be calculated from the derivation given in Section 3.1. However this procedure is sensitive to noise and also assumes that the wind has been blowing sufficiently long to saturate the directional spectrum.

### **Relating by Position**

The position of the second order peaks on the Doppler axis depends only on operating frequency and wind speed. Since the directional factor of the wave spectrum is not a function of frequency, it does not affect the location of the spectral peak. It only scales the *value* of the spectral peak. Hence the two constituent parameters  $\theta_w$  and  $s$  need not be known to relate the wind speed to the location of the second order peak on the Doppler axis.

### 3.3 Differentiating the Second Order Cross Section

From elementary calculus, the derivative of any continuous function is zero at a local maximum. The location of the maximum of a second order cross section is of interest. The expression given in equation (2.17) can be differentiated with respect to the Doppler frequency. By setting the result to zero, an expression can be derived which relates the wind speed to the position of the second order peak on the Doppler axis.

In attempting to differentiate the second order cross section, several approximations must be made. Underlying these approximations is the knowledge that the range of the typical locations of the second order peaks is given by

$$0.95\omega_B \leq \omega_{peak} \leq 0.75\omega_B . \quad (3.5)$$

Figure 3.2 shows the contours of constant Doppler which constrain the vectors  $\vec{K}_1$  and  $\vec{K}_2$ .

#### **$K_2$ is roughly constant**

For this region of interest,  $K_2$  is typically much larger than  $K_1$  and roughly constant over the range of  $\theta_{K_1}$ .  $K_2$  will be roughly the same magnitude regardless of how the vector  $\vec{K}_1$  is arranged along the contour. Furthermore, this magnitude is roughly that of the Bragg wave vector  $K = 2k_0$ . To show this mathematically, the cosine law of equation (2.19) is rearranged as a completed square:

$$(K_1 - K \cos \theta_{K_1})^2 + K \sin^2 \theta_{K_1} = K_2^2 . \quad (3.6)$$

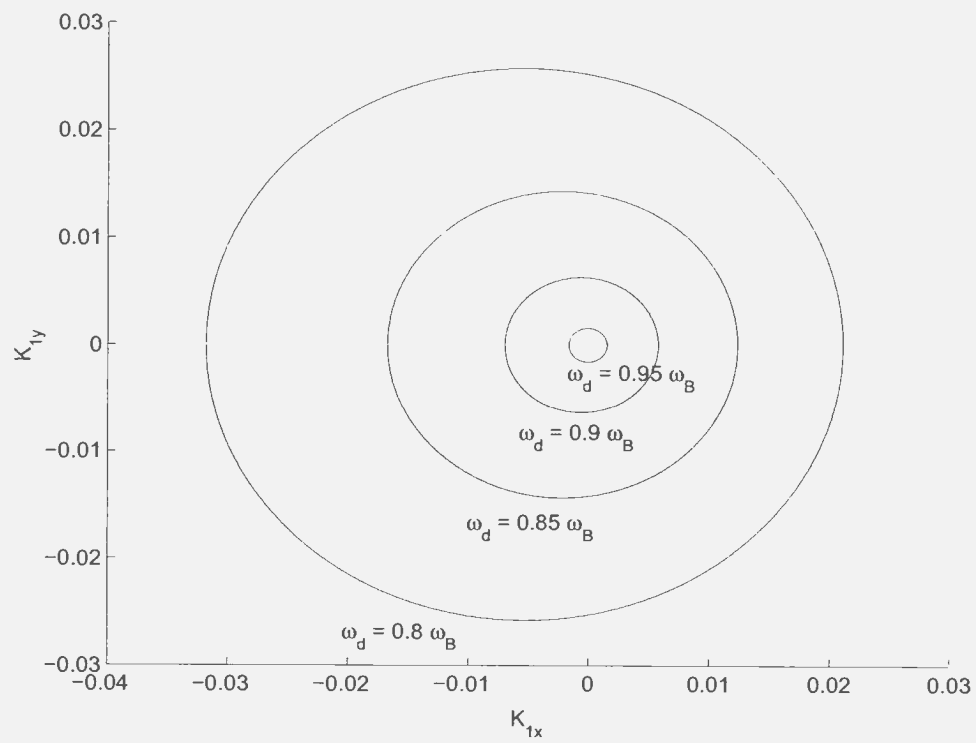


Figure 3.2: Contours of constant Doppler.

Next, the delta constraint of equation (2.18) is solved for  $K_1$  and substituted into the above

$$\left( \frac{(\omega_d + m_2 \sqrt{gK_2})^2}{g} - K \cos \theta_{K_1} \right)^2 + K^2 \sin^2 \theta_{K_1} = K_2^2. \quad (3.7)$$

Next assume the Doppler frequency is very close to the Bragg frequency; that is  $\omega_d = (1 + \epsilon)\omega_B$  where  $\epsilon < 1$  and  $\epsilon^2 \approx 0$ . Substituting this into the above and dividing both sides by  $K^2$  gives the following

$$\left( \frac{((1 + \epsilon)\omega_B + m_2 \sqrt{gK_2})^2}{gK} - \cos \theta_{K_1} \right)^2 + \sin^2 \theta_{K_1} = \left( \frac{K_2}{K} \right)^2. \quad (3.8)$$

It is known that  $\omega_B^2 = gK$ , hence

$$\left( \left( (1 + \epsilon) + m_2 \sqrt{\frac{K_2}{K}} \right)^2 - \cos \theta_{K_1} \right)^2 + \sin^2 \theta_{K_1} = \left( \frac{K_2}{K} \right)^2. \quad (3.9)$$

When  $\omega_B$  is positive,  $m_2 = -1$ , and when  $\omega_B$  is negative,  $m_2 = 1$ . The assertion

$$K_2 \approx K \quad (3.10)$$

is now made, leading to

$$(\epsilon^2 - \cos \theta_{K_1})^2 + \sin^2 \theta_{K_1} = 1. \quad (3.11)$$

Suppressing the  $\epsilon^2$  term above results in a well-known trigonometric identity, and thus consistency is verified. Since  $K_2 \approx K = \text{constant}$ ,  $dK_2 = 0$ .

### **$K_1$ is constant over angular integral**

As is seen in Figure 3.2, the frequency contours for frequencies near the Bragg frequency trace out nearly circular loci. As the Doppler frequency increases, these loci

become more and more eccentric. For the region of interest, circular loci can be assumed. Treating the cosine law of equation (2.19) as a quadratic in  $K_1$ ,  $K_1$  can be solved for explicitly via

$$K_1 = K \cos \theta_{K_1} - \sqrt{K^2 \cos^2 \theta_{K_1} - (K^2 - K_2^2)}. \quad (3.12)$$

Only the negative radical yields a possible configuration, since  $K_1 \leq K$ . Differentiating with respect to  $\theta_{K_1}$  results in

$$\frac{dK_1}{d\theta_{K_1}} = -K \sin \theta_{K_1} + \frac{K^2 \cos \theta_{K_1} \sin \theta_{K_1}}{\sqrt{K^2 \cos^2 \theta_{K_1} - (K^2 - K_2^2)}}. \quad (3.13)$$

If the approximation  $K_2 \approx K$  is made here, the bracketed term in the radicand disappears. After all cancellations

$$\frac{dK_1}{d\theta_{K_1}} \approx 0. \quad (3.14)$$

Hence for the region of interest,  $K_1$  is roughly independent of  $\theta_{K_1}$ . Figure 3.3 shows the variation of  $K_1$  with  $\theta_{K_1}$  for different Doppler frequencies. Note that this approximation becomes less valid for lower magnitude Doppler frequencies. For a Doppler frequency of  $0.9f_B$ , the peak error in assuming  $K_1$  is constant with respect to  $\theta_{K_1}$  is about 12 %, whereas for a Doppler frequency  $0.75f_B$  the peak error is about 30 %.

The Jacobian of the transformation is also assumed to be constant with respect to  $\theta_{K_1}$ , since it is only a function of  $K_1$ . The hydrodynamic coupling coefficient, however, cannot be assumed to be constant, since it varies significantly with respect to its mean value.

Before beginning the differentiation, several symbols are defined to simplify the algebraic manipulation.

$$J = \left. \frac{\partial Y}{\partial D_p} \right|_{\theta_{K_1}} \quad (3.15)$$

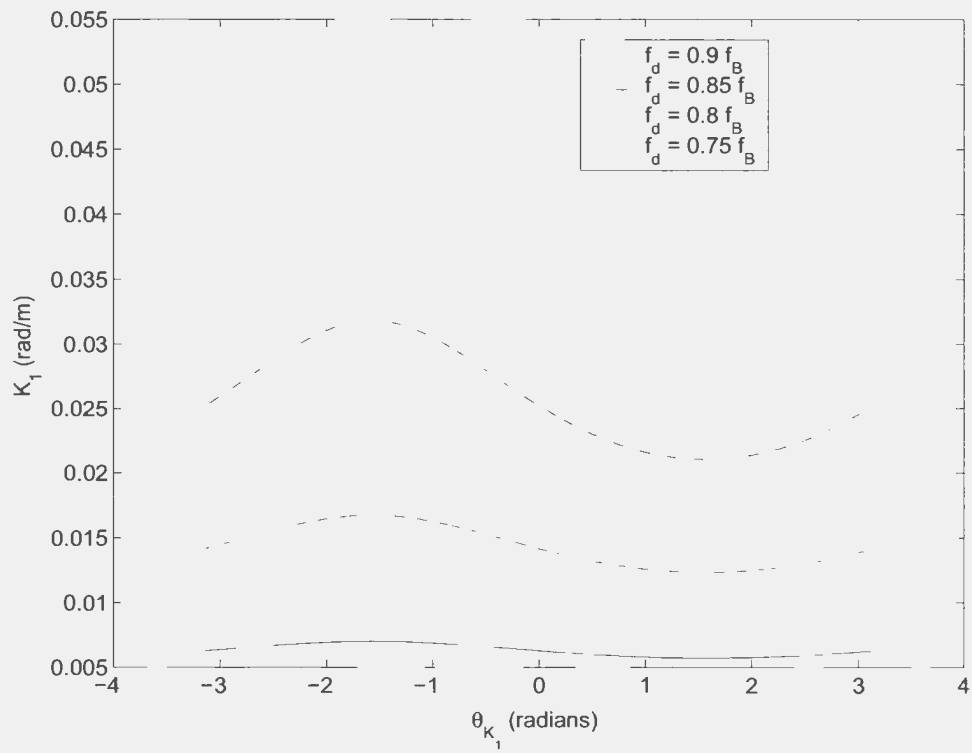


Figure 3.3:  $K_1$  versus  $\theta_{K_1}$  for different Doppler frequencies.

$$\psi = \frac{gK + (\omega_1 + \omega_2)^2}{gK - (\omega_1 + \omega_2)^2} \quad (3.16)$$

$$A = K_1 + K_2 + B \quad (3.17)$$

$$B = m_1 m_2 \sqrt{K_1 K_2} \psi \quad (3.18)$$

With these definitions, the hydrodynamic portion of the coupling coefficient  $\Gamma_H$  from equation (2.21) is now

$$\Gamma_H = \frac{j}{2} (A - B \cos(\theta_{K_2} - \theta_{K_1})) \quad (3.19)$$

The  $Y^3 = K_1^{3/2}$  factor is grouped in with the spectrum for the wave  $\vec{K}_1$ , resulting in

$$S_1(K_1) = \frac{\alpha_{PM}}{2} K_1^{-5/2} \exp\left(\frac{-0.74g^2}{K_1^2 U^4}\right) G_1(\theta_{K_1}) . \quad (3.20)$$

The spectrum for the wave  $\vec{K}_2$  is left as

$$S_2(K_2) = \frac{\alpha_{PM}}{2} K_1^{-4} \exp\left(\frac{-0.74g^2}{K_1^2 U^4}\right) G_2(\theta_{K_2}) . \quad (3.21)$$

With these substitutions the second order cross section of equation (2.17) becomes

$$\sigma_{2P} = C \int_{-\pi}^{\pi} S_1 S_2 |\Gamma_H|^2 \beta d\theta_{K_1} \quad (3.22)$$

where  $C = 2^7 \pi^2 k_0^4$ . It was mentioned earlier in this chapter that the directional factors  $G_1(\theta_{K_1})$  and  $G_2(\theta_{K_2})$  have no effect on the location of the peak, so these can be treated as constants for the purposes of this discussion and absorbed into a new constant  $C' = C G_1 G_2$ . Now the factors  $S_1$ ,  $S_2$ , and  $\beta$  are approximately independent of  $\theta_{K_1}$  and can therefore be taken outside of the integral. Expanding the  $|\Gamma_H|^2$  term

results in

$$\begin{aligned} \sigma_{2P} = & C' S_1 S_2 \beta \left[ A^2 \int_{-\pi}^{\pi} d\theta_{K_1} - 2AB \int_{-\pi}^{\pi} \cos(\theta_{K_2} - \theta_{K_1}) d\theta_{K_1} \right. \\ & \left. + B^2 \int_{-\pi}^{\pi} \cos^2(\theta_{K_2} - \theta_{K_1}) d\theta_{K_1} \right] \end{aligned} \quad (3.23)$$

since  $A$  and  $B$  are also roughly independent of  $\theta_{K_1}$ . It is inferred from Figure 2.4 that the angle  $\theta_{K_2}$  is approximately the same no matter what the arrangement of the wave vector  $\vec{K}_1$ . The integrations therefore evaluate to  $2\pi$ ,  $0$ , and  $\pi$  respectively, yielding

$$\sigma_{2P}(\omega_d) = \pi C' S_1 S_2 \beta [2A^2 + B^2] = \pi C S_2(K_2) S_1(K_1) \beta(K_1) R(K_1) \quad (3.24)$$

The factor  $S_2(K_2)$  will be constant since its argument is roughly constant. All other factors are functions of  $K_1$ , so that differentiating  $\sigma_{2P}$  with respect to  $\omega_d$  results in

$$\begin{aligned} \frac{d\sigma_{2P}(\omega_d)}{d\omega_d} = & \pi C' S_2 \left[ \frac{dS_1(K_1)}{dK_1} \beta(K_1) R(K_1) + S_1(K_1) \frac{d\beta(K_1)}{dK_1} R(K_1) \right. \\ & \left. + S_1(K_1) \beta(K_1) \frac{dR(K_1)}{dK_1} \right] \frac{dK_1}{d\omega_d} = 0 \end{aligned} \quad (3.25)$$

From the delta constraint in equation (2.18), and the fact that  $K_2$  is constant

$$\frac{dK_1}{d\omega_d} = \frac{2}{m_1} \sqrt{\frac{K_1}{g}} \quad (3.26)$$

which is nonzero. Differentiating the  $S_1(K_1)$  term with respect to  $K_1$  results in

$$\frac{dS(K_1)}{dK_1} = \left( \frac{1.48g^2}{U^4 K_1^3} - \frac{2.5}{K_1} \right) S_1 \frac{dK_1}{d\omega_d} = F(K_1, U) S_1(K_1). \quad (3.27)$$

Thus,  $S_1(K_1)$  appears in each bracketed term of equation (3.25). Factoring this out, and dividing both sides by the non-zero constants  $C'$ ,  $S_2(K_2)$ ,  $S_1(K_1)$ , and  $dK_1/d\omega_d$

yields

$$F(K_1, U)\beta(K_1)R(K_1) + \frac{d\beta(K_1)}{dK_1}R(K_1) + \beta(K_1)\frac{dR(K_1)}{dK_1} = 0 \quad (3.28)$$

Or, solving for  $F(K_1, U)$

$$F(K_1, U) = -\frac{\beta'(K_1)}{\beta(K_1)} - \frac{R'(K_1)}{R(K_1)} \quad (3.29)$$

where primed functions indicated differentiation with respect to  $K_1$ . The function  $F(K_1, U)$  can now be inverted to find an expression for the wind speed  $U$ . The delta constraint of equation (2.18), along with the fact that  $\sqrt{gK_2} \approx \omega_B$ , is used to find  $K_1$  from the Doppler frequency where the second order peak occurs.

$$K_1 = \frac{(\omega_d + m_2\omega_B)^2}{g} \quad (3.30)$$

Figure 3.4 shows a plot of equation (3.29), as well as a plot of the locations of spectral peak locations from the second order model for differing wind speeds. The second order peak used in this plot is the one immediately to the right of the receding (negative) Bragg peak, with  $f_B = 0.3951$  Hz and a radar operating frequency of  $f_0 = 15$  MHz.

The slope of this graph becomes large for higher wind speeds. This means that a small error in locating the Doppler frequency of the second order peak results in a larger error in the calculated value for the wind speed. It was found that  $U = 30$  m/s = 108 km/h was the practical limit for wind speed extraction via this method. However, the maximum wind speed recoverable is more limited by radar saturation [6]. Conversely, for lower wind speeds, the approximation made in equation (3.10) becomes less valid. This is seen in Figure 3.4 where the two plots diverge more for low wind speeds. However, it should be noted that for very low wind speeds, the second order peaks become less discernable from the radar return.

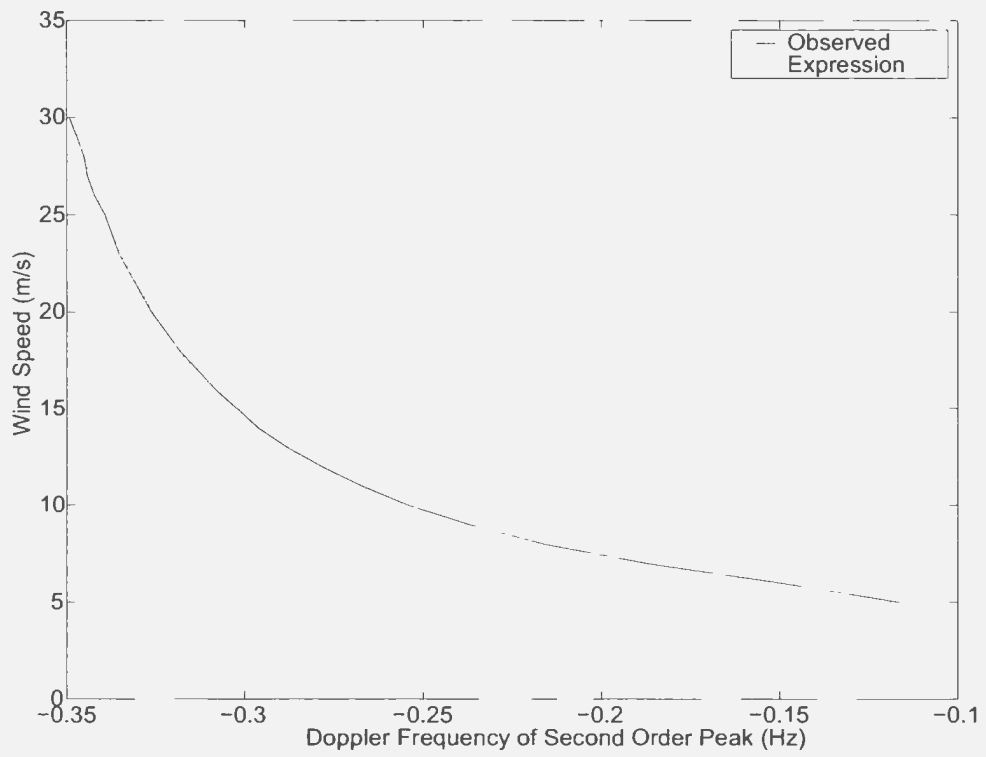


Figure 3.4: Wind speed as a function of second order Doppler peak.

It should also be noted that this derivation has only taken into consideration the second order, double patch scatter cross section of the radar return. Theoretically, the peaks in question could be contaminated somewhat by the first order cross section and the other second order cross sections. However, it is found [19] that the second order, double patch scatter cross section is much larger at the peaks than all of the other cross sections.

One nice advantage of this method is that there are up to four second order peaks to work with. Equation (3.29) can be used for the four different peaks by varying the parameters  $m_1$  and  $m_2$  to reflect the Doppler regions from which they are taken (see equation (2.20)). Hence,  $U$  can be calculated for the four different peaks and average the results to get an overall more accurate estimate for the wind speed. Also, note that a similar procedure can be used for any ocean wave spectrum model - not just the Pierson-Moskowitz spectrum - to derive an equation that relates Doppler frequency to wind speed.

## Chapter 4

# Spectral Growth

In Sections 3.1 and 3.2 methods have been outlined for extracting the wind direction and wind speed from a given radar cross section. A major constraint on these methods is the assumption that the wind has been blowing sufficiently long to result in a fully developed sea. It is therefore entirely possible that the radar can take a snapshot of the sea state in a particular locale where a given wind speed has been blowing for a time *less* than that required for full development, resulting in an inaccurate measurement. From a given snapshot, it is impossible to tell if the generating wind speed is weaker and has been blowing for a long time, or if a much stronger wind speed has been blowing for a shorter time. Compounding the difficulty is the wind direction. A stronger wind will cause the propagation direction of the ocean waves to shift more quickly.

The quantity of interest in this chapter is the ocean *spectral peak frequency*; that is, the frequency at which the ocean spectrum is a maximum. Through straightforward differentiation of equation (2.5) with respect to wave frequency, the wind speed for a *fully developed* sea is found to be related to the spectral peak frequency via

$$f_p = \frac{0.14g}{U_{19.5}} \quad (4.1)$$

Hence for a wind speed reading extracted from a radar return, the spectral peak for the illuminated patch of the ocean can be found. Note that the wind speed in most oceanographic models is normally measured from ten metres above sea level, and denoted simply as  $U$ . Using the logarithmic profile of wind speed above the sea surface [40], an expression for  $U$  in terms of the Pierson-Moskowitz peak frequency is obtained as

$$f_p \approx \frac{0.13g}{U} \quad (4.2)$$

The total energy density of the wave spectrum is also of interest. This is found by integrating equation (2.5) over all frequencies:

$$E_{PM} = \int_0^\infty F(f)df = \frac{\alpha_{PM}g^2}{5(2\pi f_p)^4} \quad (4.3)$$

## 4.1 Description of spectral growth

A constant wind speed blowing over a hypothetically calm extent of ocean (called the *fetch*), will result in small waves due to the pressure fluctuations caused by the turbulent flow of air over the ocean surface. Pressure differences resulting from the wind blowing over these small waves will then cause them to grow. This is an unstable process since larger waves cause larger pressure differences [23]. Nonlinear effects between these pressure-induced waves will then result in longer, lower frequency waves [41]. The peak frequency of the ocean wave spectrum therefore decreases with time. Eventually, the sea spectrum will saturate and no further wave growth will occur. This is precisely what the Pierson-Moskowitz spectrum of equation (2.5) reflects.

In the case that the wind has not been blowing over the fetch for a sufficiently long time to saturate the spectrum, the spectrum is said to be *duration limited*.

Two notable studies have explicitly examined duration limited growth: the Shore Protection Manual (SPM) of the U. S. Army Coastal Engineering Research Centre (CERC) [30], [42] and the JONSWAP project [24]. The results of these studies can be used to construct curves of spectral peak frequencies as functions of time and wind speed. Before describing these methods, several parameters must be defined [43]. The *non-dimensional fetch*  $\chi$  is given by

$$\chi = \frac{gX}{U^2} \quad (4.4)$$

where  $X$  is the length of the fetch. The *non-dimensional duration*  $\varsigma$  is given by

$$\varsigma = \frac{gt}{U} \quad (4.5)$$

where  $t$  is the duration for which the wind speed has been blowing in seconds. Finally, the *non-dimensional frequency*  $\nu$  is given by

$$\nu = \frac{f_p U}{g} \quad (4.6)$$

The 1977 SPM by CERC [30] gives a relation between  $\varsigma$  and  $\chi$  as

$$\varsigma = 6.5882 \exp \left[ \sqrt{0.0161 \ln^2 \chi - 0.3692 \ln \chi + 2.2024} + 0.8798 \ln \chi \right] \quad (4.7)$$

The non-dimensional frequency is given by:

$$\nu = \frac{0.133}{\tanh(0.077\chi^{0.25})}; \quad (4.8)$$

Thus, equation (4.7) can be solved for different values of  $\varsigma$  from equation (4.5), and the spectral peak frequency  $f_p$  can be recovered via equation (4.8) and equation (4.6).

The JONSWAP results [24] give a much simpler relation between  $\chi$  and  $\varsigma$  as

$$\chi = \left( \frac{\varsigma}{68.8} \right)^{3/2} \quad (4.9)$$

and a correspondingly simpler expression for the non-dimensional frequency as

$$\nu = 3.5\chi^{-0.33} \quad (4.10)$$

It is easily deduced from equations (4.10), (4.9), (4.5), (4.6), and (4.4) that

$$f_p = 29.0 \sqrt{\frac{g}{U}} t^{-\frac{1}{2}} \quad (4.11)$$

The 1984 SPM by CERC [42] gives a slightly different variation of the JONSWAP method, whereby the non-dimensional fetch and duration are given by

$$\chi = \frac{gX}{U_A^2} \quad (4.12)$$

and

$$\varsigma = \frac{gt}{U_A} \quad (4.13)$$

where  $U_A = 0.71U^{1.23}$  is the so-called adjusted wind speed. From equations (4.10), (4.9), (4.13), (4.6), and (4.12),  $f_p$  may be explicitly expressed as

$$f_p = 30.7 \sqrt{gt}^{-\frac{1}{2}} U^{-0.54} \quad (4.14)$$

which, upon comparison, is not appreciably different from equation (4.11).

Plots of spectral peak frequency as functions of time and wind speed, from both the 1977 SPM and JONSWAP project, are given in Figure 4.1. Note that there is definite discrepancy between the two curves, but both show the near-asymptotic approach of

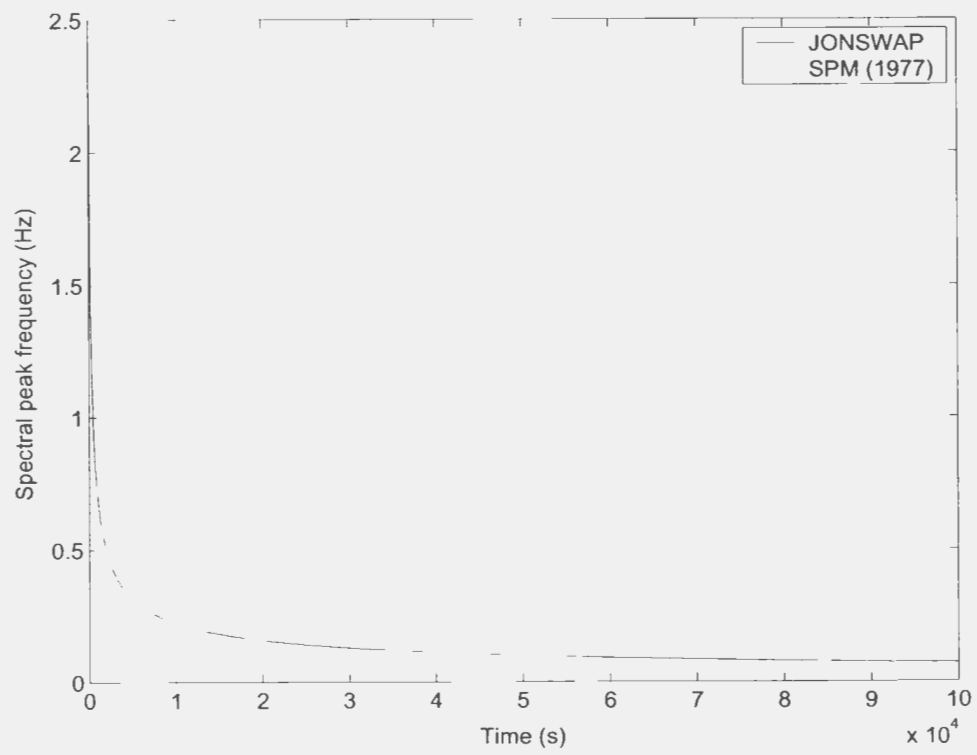


Figure 4.1: JONSWAP and SPM growth curves.

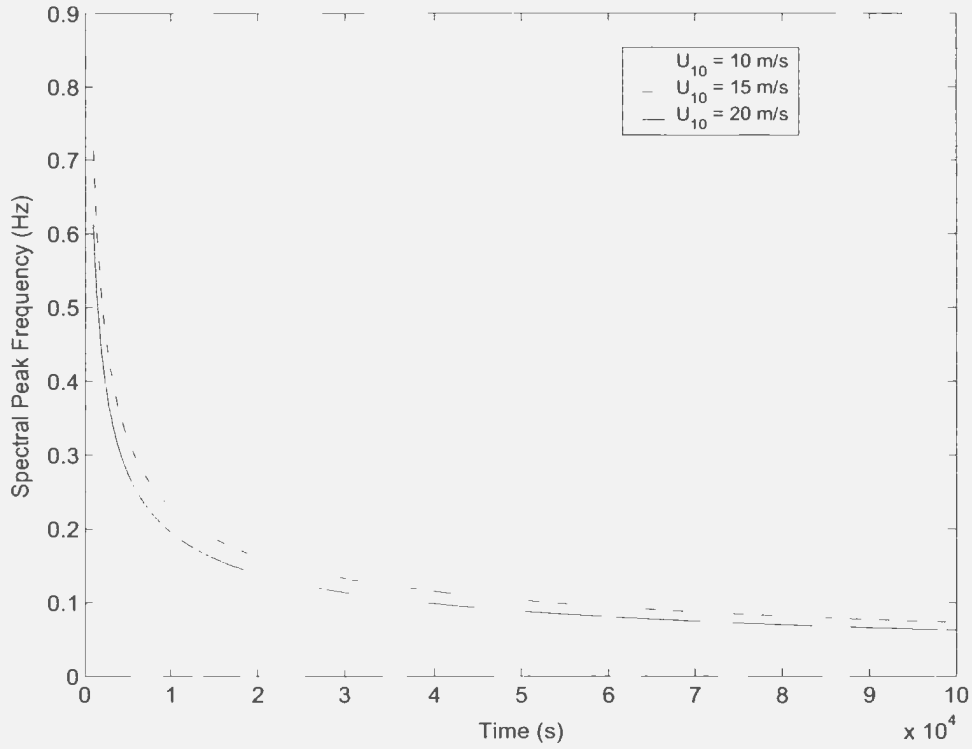


Figure 4.2: JONSWAP growth curves for different wind speeds.

the spectral peak to a saturated value. A plot of the JONSWAP growth curves for different wind speeds is given in Figure 4.2. This demonstrates that the wind speed dictates not only the saturation value but the *rate of change* of the spectral peak. Stronger winds will cause the spectral peak to change more quickly during early stages of sea development. Hence, given a peak frequency, and a time derivative of the peak frequency, a wind speed reading can be recovered at *any* stage of the spectral growth process.

Straightforward differentiation of equation (4.11) results in

$$\dot{f}_p = \frac{\partial f_p}{\partial t} = -14.5 \sqrt{\frac{g}{U}} t^{-\frac{3}{2}} \quad (4.15)$$

Solving equation (4.11) for  $t$  and substituting into equation (4.15), an explicit expression for  $U$  is found as

$$U = -1687.4 \frac{g f_p}{f_p^3} \quad (4.16)$$

## 4.2 Numerical spectrum growth techniques

The spectral energy balance equation, commonly used in physical oceanography, is given by

$$\frac{\partial F(f, \theta)}{\partial t} + C_g \cdot \nabla F(f, \theta) = S_{tot} \quad (4.17)$$

where  $F(f, \theta)$  is the directional ocean wave spectrum.  $C_g$  is the group velocity of the ocean waves, also known as the *celerity* of the waves. It has been shown that for large fetches, the  $C_g \cdot \nabla F(f, \theta)$  term vanishes. This is because the ocean spectrum under these conditions is not dependent on position.  $S_{tot}$  is the total spectral energy change, given by the sum

$$S_{tot} = S_{in} + S_{ds} + S_{nl} \quad (4.18)$$

Each of the terms on the right hand side of equation (4.18) represents a physical process responsible for spectral growth and decay:

$S_{in}$  is the energy input from the atmosphere to the wave spectrum.

$S_{ds}$  represents energy dissipated from the spectrum via mechanisms such as white-capping.

$S_{nl}$  is the energy transfer from one portion of the spectrum to another because of non-linear wave-wave interactions.

The non-linear transfer term is crucial in developing third generation wave models. Its evaluation is extremely computationally demanding, even when employing the simplification techniques outlined in [33]. Fortunately, the *shape* of the spectrum as

it grows is not of particular interest, but rather only the amount of energy in the spectrum, which is directly related to the spectral peak frequency. Also, the non-linear term is conservative: it only transfers energy from one portion of the spectrum to another [40]. As such its average value is zero across all frequencies. If both sides of equation (4.17) are integrated over all frequencies, the  $S_{nl}$  term vanishes, giving

$$\int_0^{\infty} \frac{\partial F(f, \theta)}{\partial t} df = \int_0^{\infty} (S_{in} + S_{ds}) df . \quad (4.19)$$

Many different forms for  $S_{in}$  have been proposed. The form of choice here is that used in the EXACT-NL model [31] as given by

$$S_{in} = \begin{cases} 0.25 \frac{\rho_a}{\rho_w} \left( \frac{U \cos \theta_w}{c} - 1 \right) \omega F(f, \theta) & U \cos \theta_w > c \\ 0 & U \cos \theta_w < c \end{cases} \quad (4.20)$$

where  $\rho_a$  and  $\rho_w$  are the respective densities of air and seawater,  $\theta_w$  is the angle between the wind direction and the wave propagation direction, and  $c = g/\omega$  is the phase velocity of the wave.

As with  $S_{in}$ , many different forms of  $S_{ds}$  have been proposed, and again the form used in [31] will be used:

$$S_{ds} = -1.2 \times 10^9 \alpha^6 \omega_p^{-3} \omega^4 F(f, \theta) \quad (4.21)$$

With the intention of numerically integrating equation (4.19) with respect to time, the partial derivative is replaced with its discrete approximation

$$\int_0^{\infty} \frac{F'(f, \theta) - F(f, \theta)}{\Delta t} df = \int_0^{\infty} (S_{in} + S_{ds}) df \quad (4.22)$$

Note that the left hand side of equation (4.22) is simply the difference of energy in the spectra  $F'$  and  $F$ . Substituting equation (4.3) into equation (4.22), and solving

explicitly for the energy of the new spectrum

$$E' = E + \Delta t \int_0^{\infty} (S_{in} + S_{ds}) df . \quad (4.23)$$

Next, the expressions for  $S_{in}$  and  $S_{ds}$ , as found in equations (4.21) and (4.20) respectively, are substituted into equation (4.23). Note that since these terms use  $\omega$  instead of  $f$ , the radial frequency form of the PM spectrum as given by

$$F(\omega) = \frac{\alpha_{PM} g^2}{\omega^5} \exp \left( -\frac{5}{4} \left( \frac{\omega}{\omega_p} \right)^4 \right) , \quad (4.24)$$

is used and the integration variable  $df = d\omega/2\pi$  is changed to get

$$E' = E + \frac{\Delta t}{2\pi} \int_0^{\infty} \left( \max \left\{ 0, 0.25 \frac{\rho_a}{\rho_w} \left( \frac{\omega U \cos \theta_w}{g} - 1 \right) \omega \right\} - 1.2 \times 10^9 \alpha^6 \omega_p^{-3} \omega^4 \right) F(\omega) d\omega . \quad (4.25)$$

The plot of peak frequency versus time is generated by choosing a time step  $\Delta t$  and calculating the new energy of the spectrum from equation (4.25) given an initial peak frequency. The new peak frequency is recovered via equation (4.3) and the process is repeated. A comparison of the growth curves resulting from the spectral energy balance equation and the JONSWAP project growth curves is presented in Figure 4.3. The chosen wind speed was  $U = 15$  m/s, and  $\theta_w = 0$ . One point of interest is that at the saturation value,

$$t = 7.15 \times 10^4 \frac{U}{g} ,$$

of the duration-limited JONSWAP curve [40], the peak frequency of the Pierson-Moskowitz spectrum which has evolved via the numerical spectrum growth techniques is consistent with the saturation value of equation (4.2).

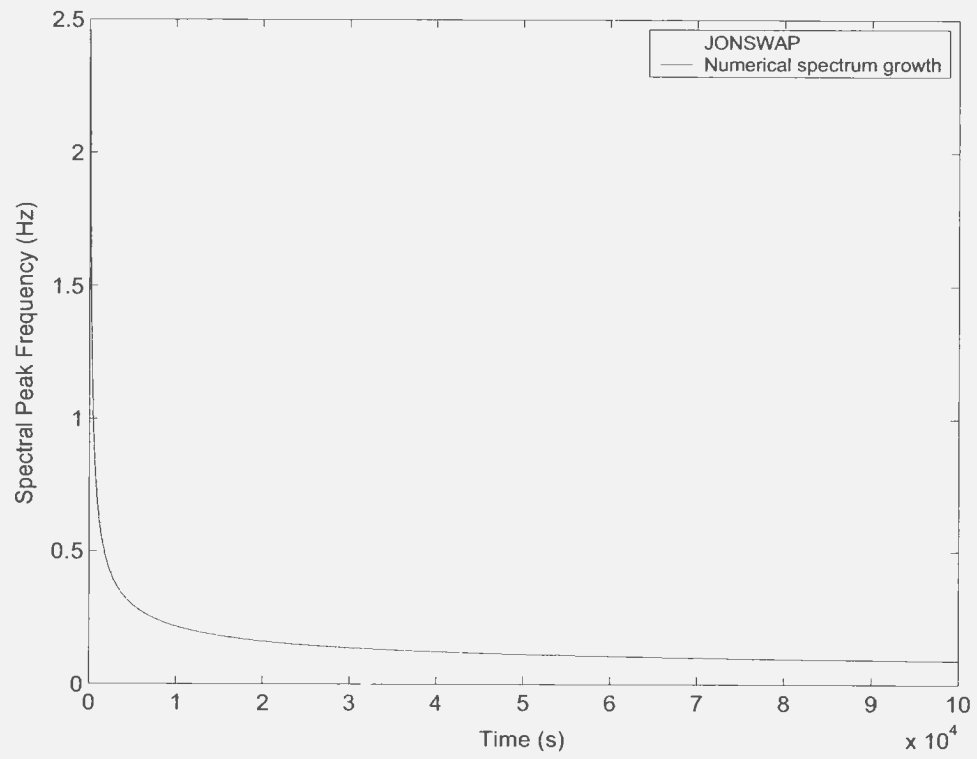


Figure 4.3: Growth curves for JONSWAP and numerical spectrum from energy balance equation.

# Chapter 5

## Tests on Simulated Noisy Data

The theory developed in Chapter 3 and Chapter 4 has assumed ideal data; that is, the effects of noise have not been accounted for. In this chapter, the robustness of these models is tested on simulated noisy data which is generated as outlined in Section 2.4. Various signal processing techniques are also mentioned that will condition the noisy data for use in these models.

### 5.1 Extracting Simulated Wind Speed

In Section 3.2 an equation was derived that related the location of the second order peaks on the Doppler axis to the saturated wind speed. As can be seen from Figure 3.4, a slight error in locating the second order peak can result in a large error in the calculated wind speed, especially for peaks located nearer to the Bragg frequency. It is obvious that noise may threaten the effectiveness of this expression.

Figure 5.1 shows a typical simulated noisy cross section for a radar operating at 25 MHz and with a wind speed of 15 m/s and a wind direction of  $90^\circ$  to the radar beam direction. The second order peaks are not discernable from this cross section, and hence signal processing is required. A logical approach would be to take many of these noisy cross sections and average them, with the hope that the contribution

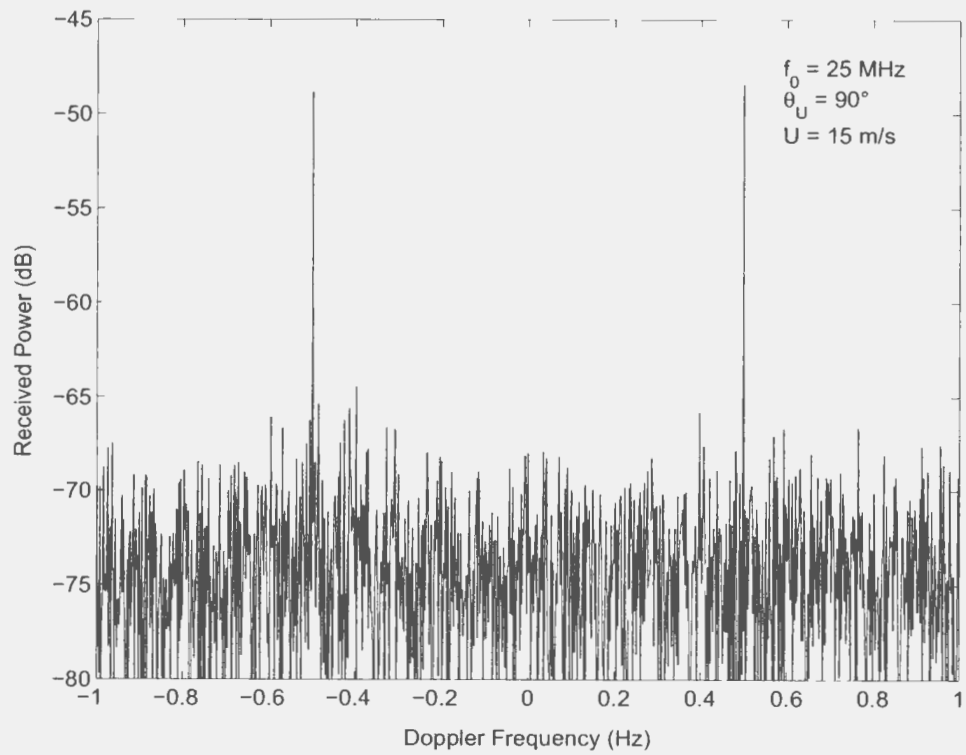


Figure 5.1: Typical simulated noisy radar Doppler spectrum.

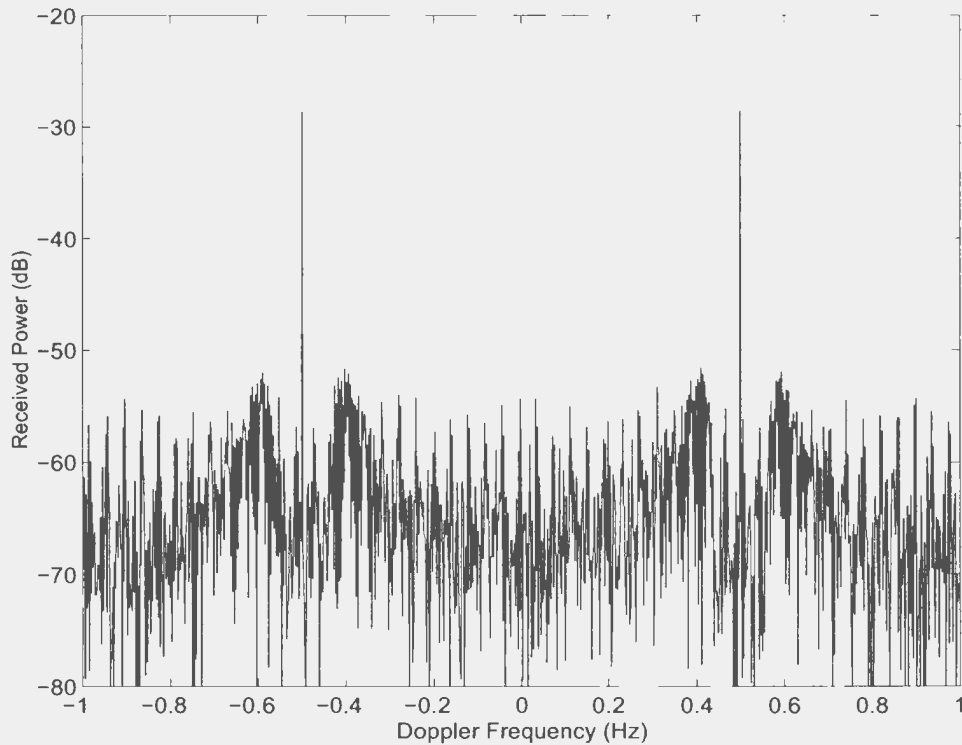


Figure 5.2: Ten averaged Doppler spectra.

of noise to the cross section will average to nearly zero. Figures 5.2 and 5.3 show the results of averaging ten and twenty-five cross sections respectively. Notice that the second order peaks are now discernable. However automated location of the peak is still difficult because of the jagged edges of the graph.

To eliminate the spectral roughness, the cross section was convolved with a Hamming window. Figures 5.4, 5.5, and 5.6 show the results of convolving 5, 10, and 15-point Hamming windows, respectively, with the twenty-five averaged spectra in Figure 5.3. Generally, the longer the window, the more pronounced the second order peaks become. The length cannot be too great, however, because then the second order peaks will be convolved with the Bragg lines.

While averaging and windowing the cross sections minimizes the impact of noise, the second order peaks are still variant: that is, the locations of the peak is still quite inconsistent among several cross sections. To address this issue, the wind speed is

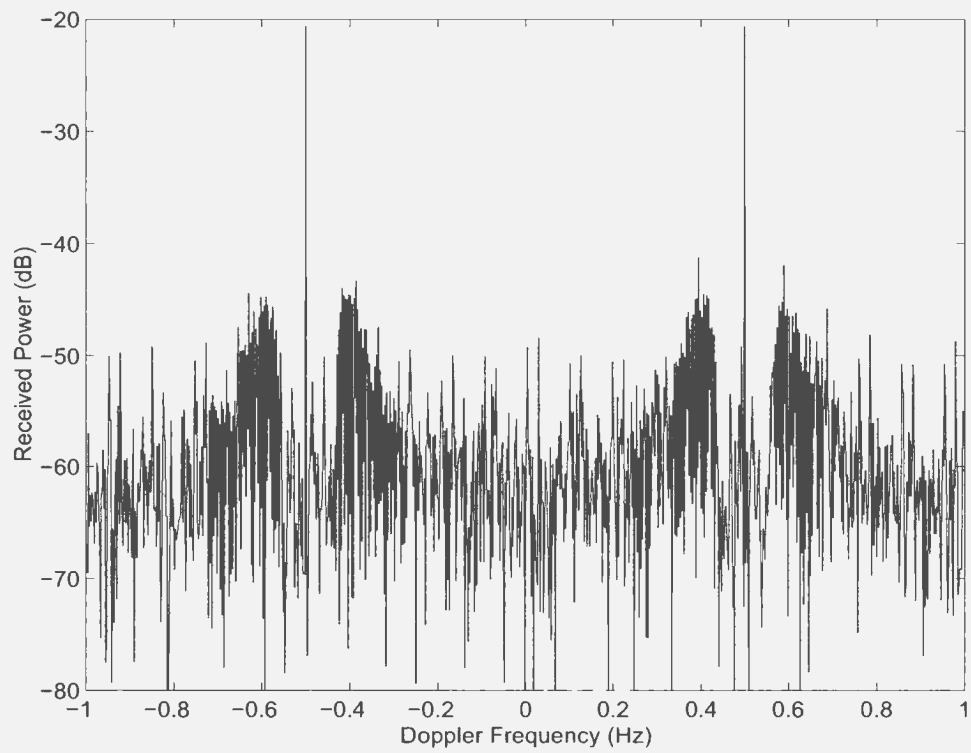


Figure 5.3: Twenty-five averaged Doppler spectra.

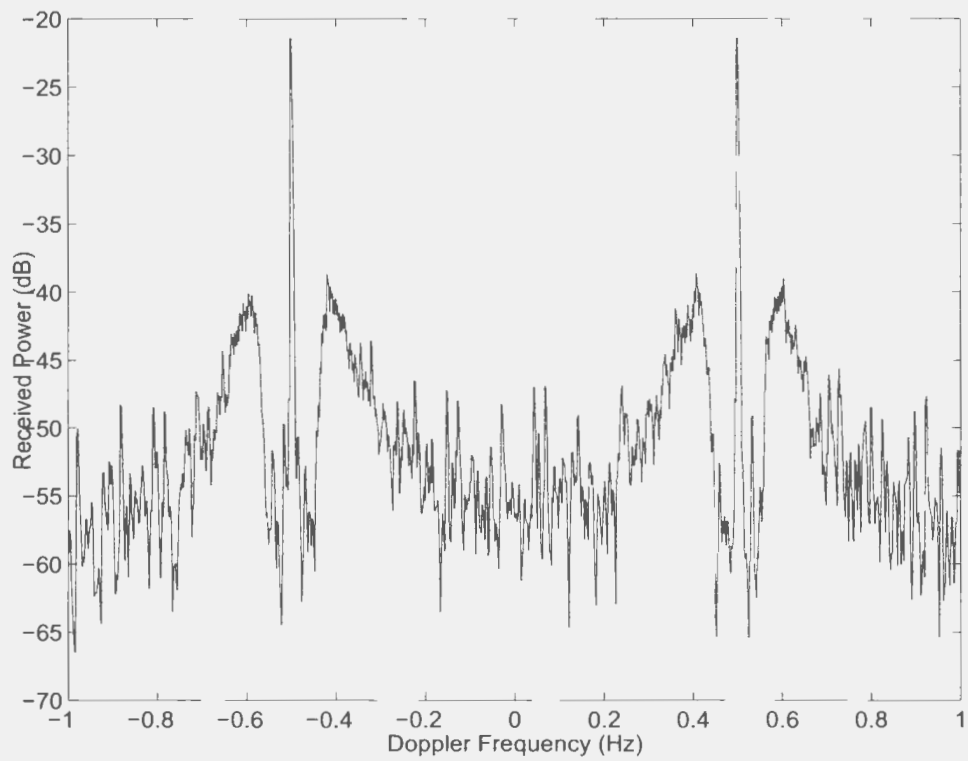


Figure 5.4: Result of a 5-point Hamming window applied to Figure 5.3.

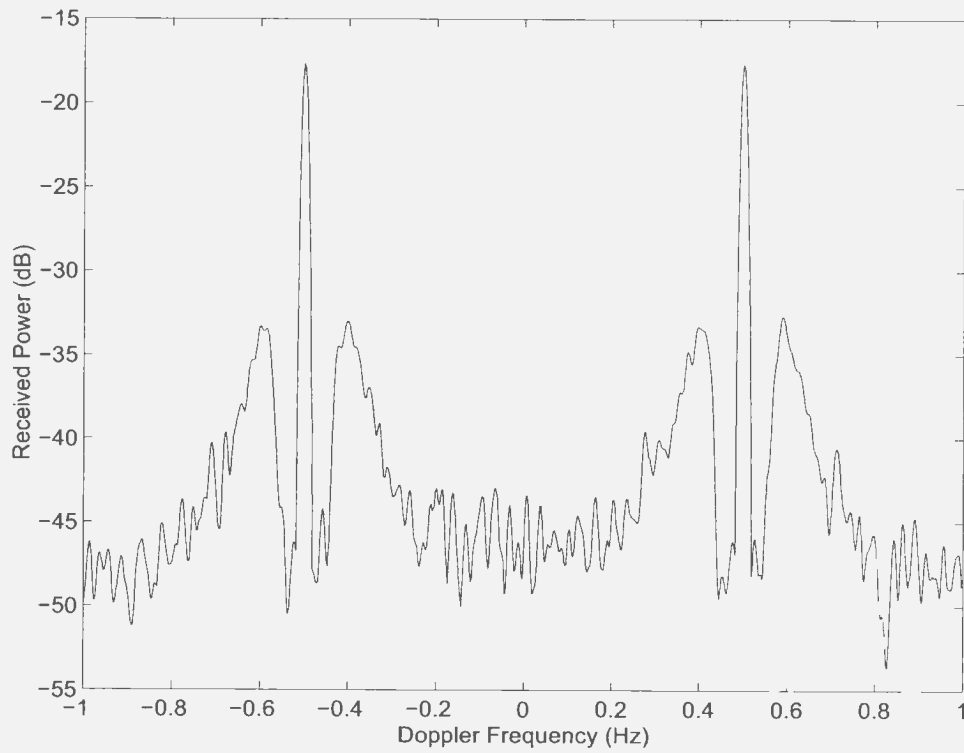


Figure 5.5: Result of a 9-point Hamming window applied to Figure 5.3.

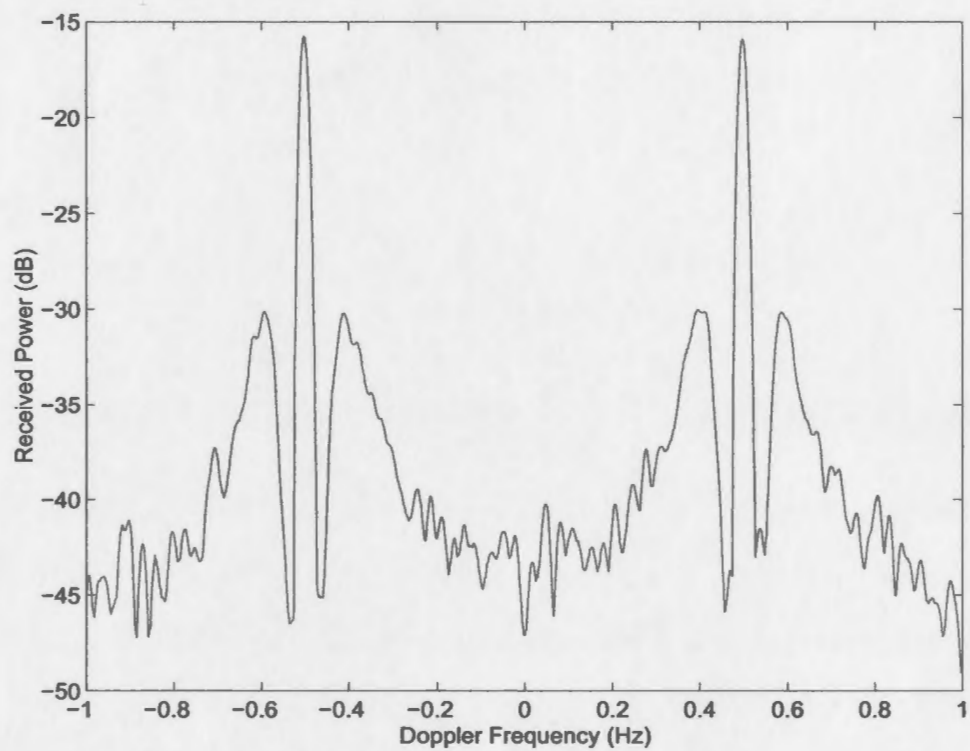


Figure 5.6: Result of a 13-point Hamming window applied to Figure 5.3.

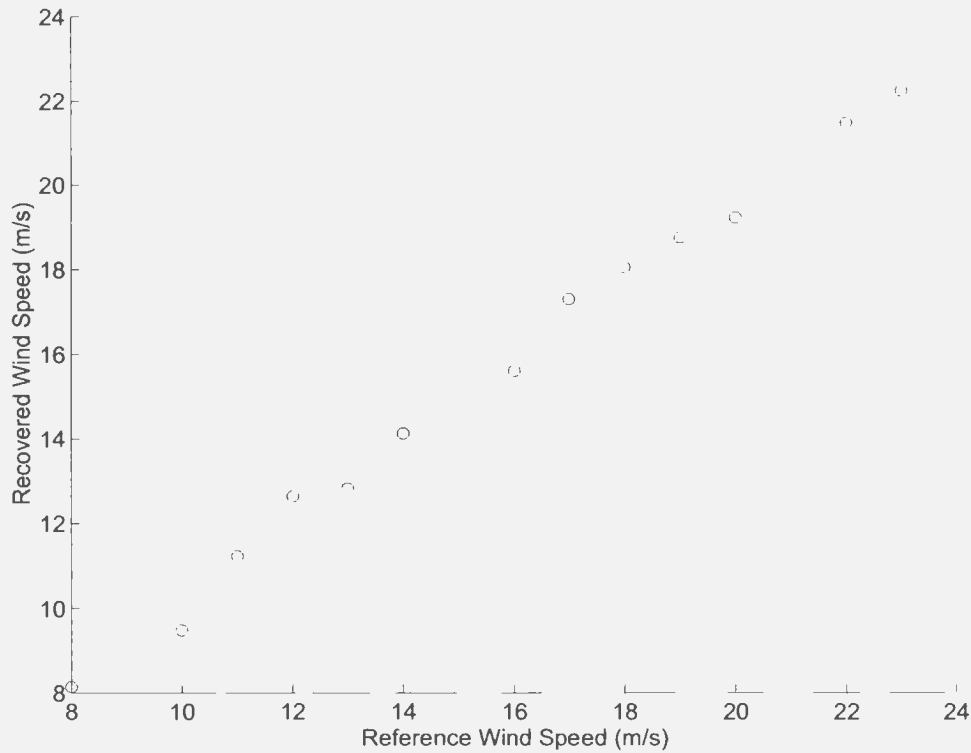


Figure 5.7: Wind speed recovered from conditioned Doppler spectra.

calculated at each of the available second order peaks, and all of the results averaged. Figure 5.7 show the results of the extraction algorithm of Section 3.2 when the above mentioned signal processing techniques are employed. Twenty-five generated cross sections were averaged for an operating frequency of 25 MHz, and this was done for wind speeds ranging from 8 m/s to 23 m/s in increments of 1 m/s. As can be seen, the results are quite good with a maximum error of less than 6%.

## 5.2 Extracting Wind Speed from Spectral Growth

In Section 4.1 a model was developed that would convert a time series of spectral peak frequencies as read from the radar spectra to a time series of wind speeds. The

governing differential equation from equation (4.16) is

$$\dot{f}_p = -\frac{U}{1687.4g}f_p^3, \quad (5.1)$$

and  $f_p$  is obtained by employing the method outlined in Section 3.2 to find  $U$  and then using

$$f_p \approx \frac{0.13g}{U} \quad (5.2)$$

It was demonstrated that  $U$  could be recovered from a typical noisy radar return to within 10%. Hence the recovered values for  $f_p$  should be recovered to 10% as well. Unfortunately, the differential equation is of order  $f_p^3$ . Hence a 10% error in measurement can result in a 33% error in calculating the wind speed. Also, since discrete differentiation is required, the errors could add up to 20% for the subtraction required in calculating  $\dot{f}_p$ . This will lead to even more significant error. A method is sought which will suppress the noise of the  $f_p(n)$  discrete time series.

One noticeable property about wind blowing over the ocean surface is that it has a very smooth distribution and sudden large changes in wind speed are unlikely. Also, the time response of the ocean to a given wind condition is quite slow, as dictated by the large denominator on the right-hand side of equation (5.1). As such, sudden changes in the spectral peak frequency  $f_p(n)$  are impossible.

Figure 5.8 shows the ocean spectral response to a wind speed of 10 m/s increasing to 15 m/s, over a period of 10,000 seconds, with an initial peak frequency of 0.4 Hz. Figure 5.9 shows the same time series distorted by a normally distributed 6% noise. That is

$$f_{p, \text{noisy}}(n) = f_p(n)[1 + \phi] \quad (5.3)$$

where  $\phi$  is a normally distributed random variable with a mean of  $\mu = 0$ . A normal distribution is chosen because the central limit theorem will apply to averaging many radar cross sections with a uniform distribution [44]. Further, the standard deviation

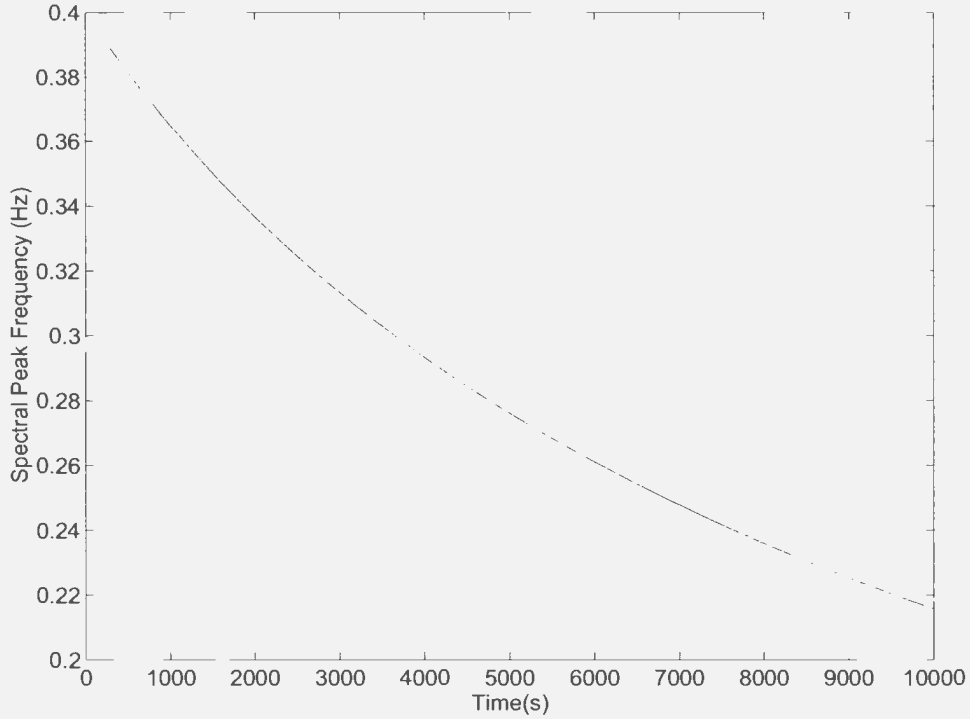


Figure 5.8: Ocean spectral growth for a wind speed of 10 m/s increasing to 15 m/s.

of the distribution of  $\phi$  is taken to be  $\sigma_\phi = 6\%/\sqrt{25} = 1.2\%$ , as per the formula in [44].

Low-pass filtering seems like an obvious solution to the problem. Applying a Hamming window or Butterworth filter indeed results in a “smoother” signal. The key problem to be addressed here is that there are only a certain range of slopes for the signal  $f_p(n)$  which represent physically possible wind conditions. Assuming a maximum wind speed of 30 m/s suddenly applied to a fairly calm sea state having an ocean spectral peak frequency of 2 Hz, this range of slopes is (from equation (5.1))

$$0 \leq \dot{f}_p \leq 0.0145 \text{ s}^{-2} \quad (5.4)$$

It is possible to find an average slope along many points using a regression line technique. This approach poses two problems. First, the result would represent the

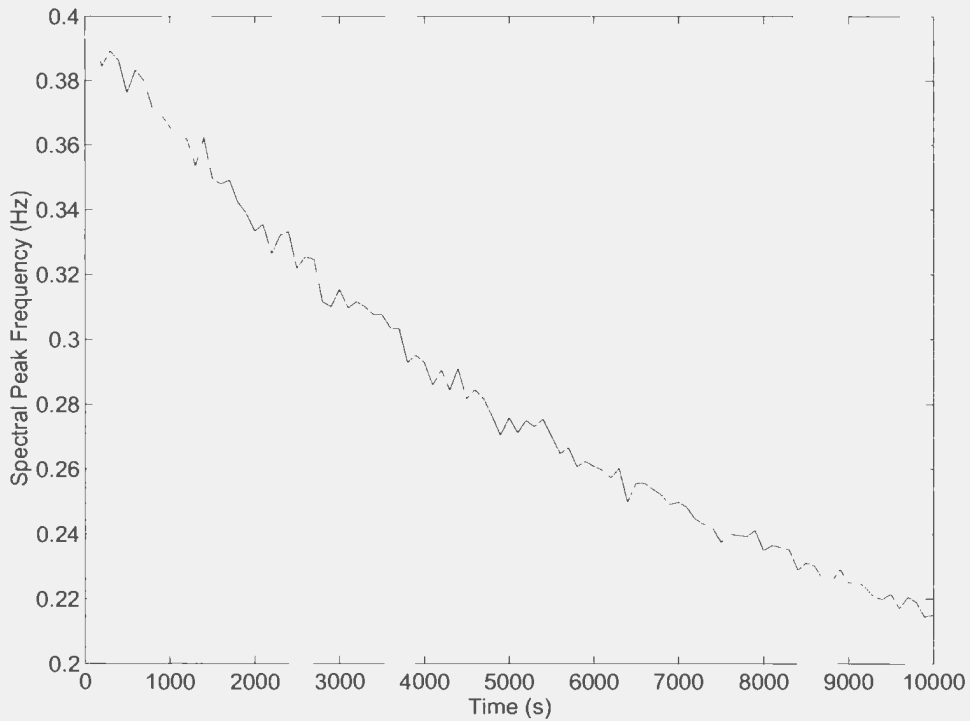


Figure 5.9: Noisy version of Figure 5.8.

*average* of the wind speeds present in the time encompassed by the  $f_p(n)$  points. Secondly, a suitable number of points must be determined. Even then it is possible to have a slope outside the acceptable range. It would therefore be preferable to generate a non-linear curve, according to the differential equation in equation (5.1), which *best* fits the given data. For this, a non-linear fitting algorithm is required, such as the Gauss-Newton least squares method [45]. The shaping parameters would be the vector of wind speeds, and an initial spectral peak frequency. The results of using this approach can be seen in Figure 5.10. As can be seen, the curve-fitting method yields acceptable results, with a peak error of roughly 20%. Note that the recovered results near the end of the time series are more deviant than those in the beginning and in the middle. This is owing to the nature of the least-squares curve fitting algorithm and the differential equation in equation (5.1). An error in an estimated wind speed toward the beginning of the time series will accumulate to a very large

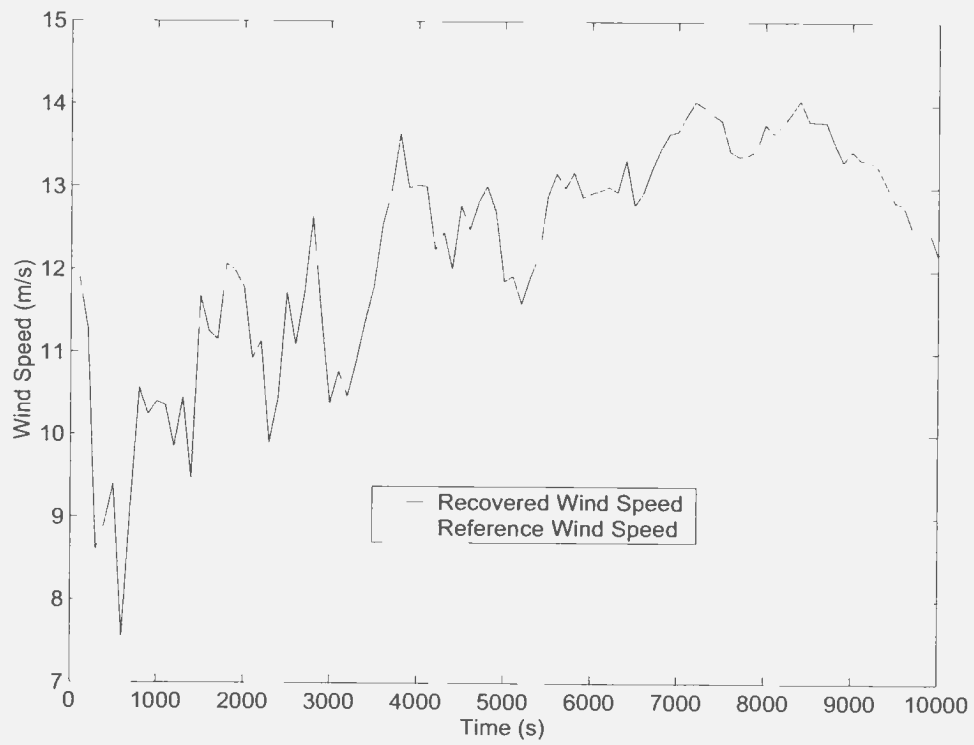


Figure 5.10: Recovered wind speed from noisy  $f_p(n)$  time series.

square error overall. In comparison, the effects of an error later in the time series will have a much smaller impact on the overall square error. Hence more importance is shifted towards the convergence of earlier time series points than later ones. Later time series points can hence be expected to be more erroneous.

## Chapter 6

### Application of Models

HF ground wave radar data were collected from a Coastal Ocean Dynamics Applications Radar (CODAR) unit that Rutgers University operates at Breezy Point, New York. The scanned patch of ocean is at  $40^{\circ}30'$  N latitude and  $73^{\circ}54'$  W longitude. The run was over a seven hour period on August 31, 2004, from 14:11:20 EDT to 21:11:39 EDT. Ground truth data were acquired from the National Oceanic and Atmospheric Administration (NOAA) website. NOAA has a weather station deployed in the Atlantic Ocean at  $40^{\circ}27'$  N latitude and  $73^{\circ}48'$  W longitude, which is very near where the Breezy Point CODAR unit operates.

Radar information was grouped in range bins of 10 km each. A Doppler spectrum was generated every 256 seconds. The data, as received, were represented as a discrete-time series of complex voltages as received by the three receiving antennas of the CODAR. Lipa and Barrick [46] have derived the relationship between the three antenna voltages as

$$\langle |V_3(\omega)|^2 \rangle = \frac{\langle |V_1(\omega)|^2 \rangle}{a_1^2} + \frac{\langle |V_2(\omega)|^2 \rangle}{a_2^2} \quad (6.1)$$

where  $V_1(\omega)$  and  $V_2(\omega)$  are the complex frequency spectra obtained from the two loop antennas, and  $V_3(\omega)$  is that of the monopole. The constants  $a_1$  and  $a_2$  are normally found by fitting the data using a least-squares algorithm [46]. With an interest in reducing computation time, only the monopole voltage will be used to construct

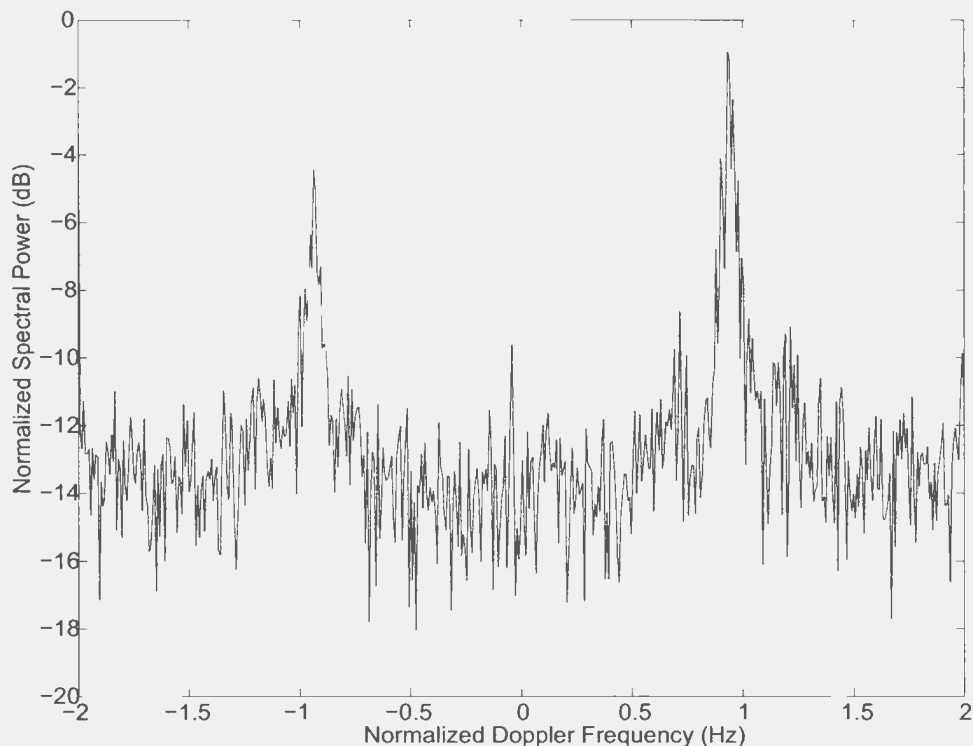


Figure 6.1: Sample cross section from Breezy Point run.

the Doppler spectra that will be used for wind speed extraction. This is a valid approach, since recall that the extraction method of Section 3.2 does not depend on the magnitude of the second order peaks, but rather their positions along the Doppler frequency axis. Figure 6.1 depicts a sample radar cross section taken from a range bin at 14:11:20 EST. As can be seen, the cross section requires the conditioning outlined in Section 5.1.

Figure 6.2 shows the same cross section convolved with a twenty-point Hamming window, with the first nine and last ten points truncated. The second order peaks are now recognizable, and it is entirely possible to apply the method outlined in Section 3.2 to obtain an assumed saturated wind speed from this cross section. First, however, the effects of surface currents must be removed from the cross section.

Surface currents result in a shift of the idealized cross section along the Doppler axis. To undo the effects of surface currents, a new zero-Doppler point must be

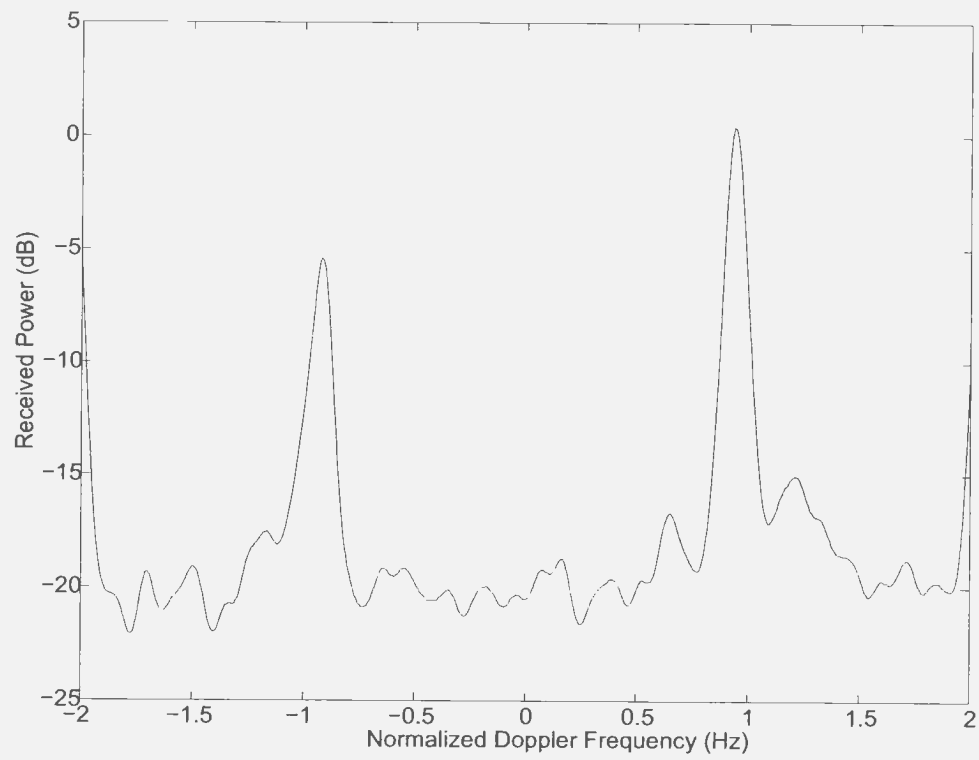


Figure 6.2: Hamming windowed cross section.

identified on the axis. Zero-Doppler occurs halfway between the two Bragg peaks when there are no surface currents present. Hence, it will be assumed that the average of the two indices representing the Doppler location of the left and right Bragg lines will be the index of effective zero-Doppler,  $n_{zero}$ . Given the indicial distance between effective zero-Doppler  $n_{zero}$  and the Bragg line  $n_B$  that is closest to the second order peak of interest, the index of the second-order peak  $n_{SOP}$  can be normalized between zero (zero-Doppler) and one (Bragg line). Mathematically, the radial Doppler frequency  $\omega_{SOP}$  of the second order peak is given as

$$\omega_{SOP} = \frac{n_{SOP} - n_{zero}}{n_B - n_{zero}} \omega_B \quad (6.2)$$

and it is this value that will be used in the method outlined in Section 3.2. Using the second order peaks identified in Figure 6.2, and reading from left to right, values of 10.57, 9.52, 9.26, and 9.33 are obtained for wind speeds in metres per second. Averaging these four quantities gives a saturated wind speed of  $U_{sat} = 9.67$  m/s, and an implied spectral peak of  $f_p = 0.1319$  Hz.

Performing this same method over all of the Doppler spectra acquired during the duration of the run, a series of  $U_{sat}$  readings is obtained and presented in Figure 6.3. Note that the trend suggests that the wind speed is increasing. This series of  $U_{sat}$  values was then converted to implied spectral peak frequencies using the relation given in equation (4.2).

Finally, a Gauss-Newton least-squares fitting algorithm was used to fit the differential equation in equation (5.1) to the radar-inferred data using 100 wind speeds corresponding to the 100 time points reflected by the data as fitting parameters. Figure 6.4 shows the spectral peaks inferred from the radar, as well as a plot of the fitted curve.

The wind speeds which were recovered via this method are shown against the

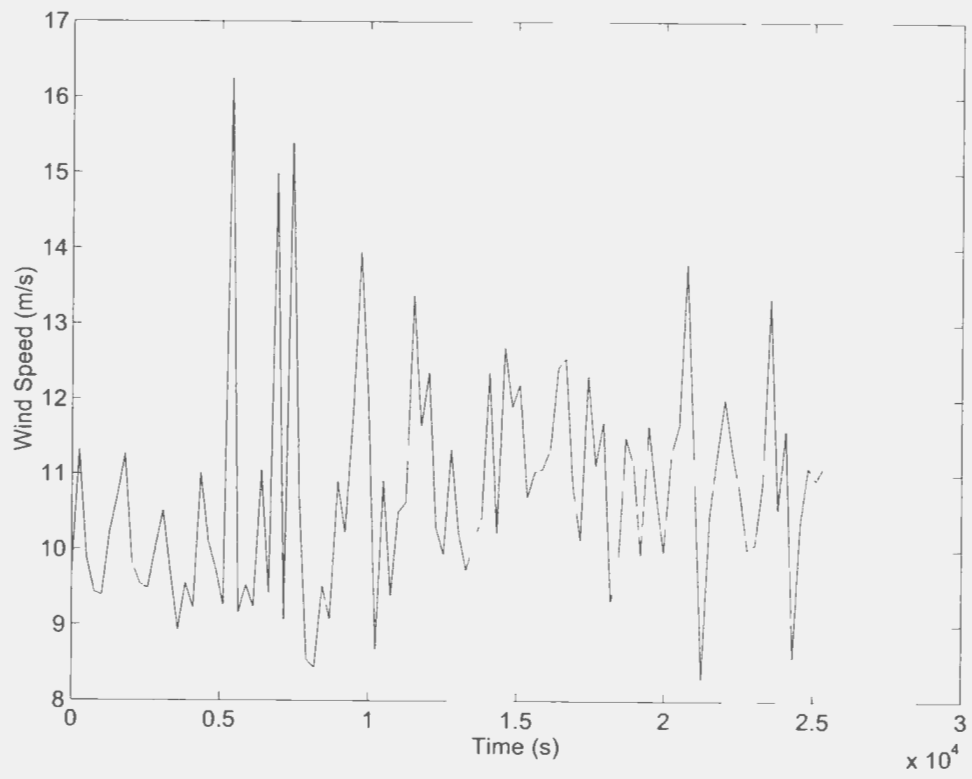


Figure 6.3: Radar-inferred saturated wind speeds.

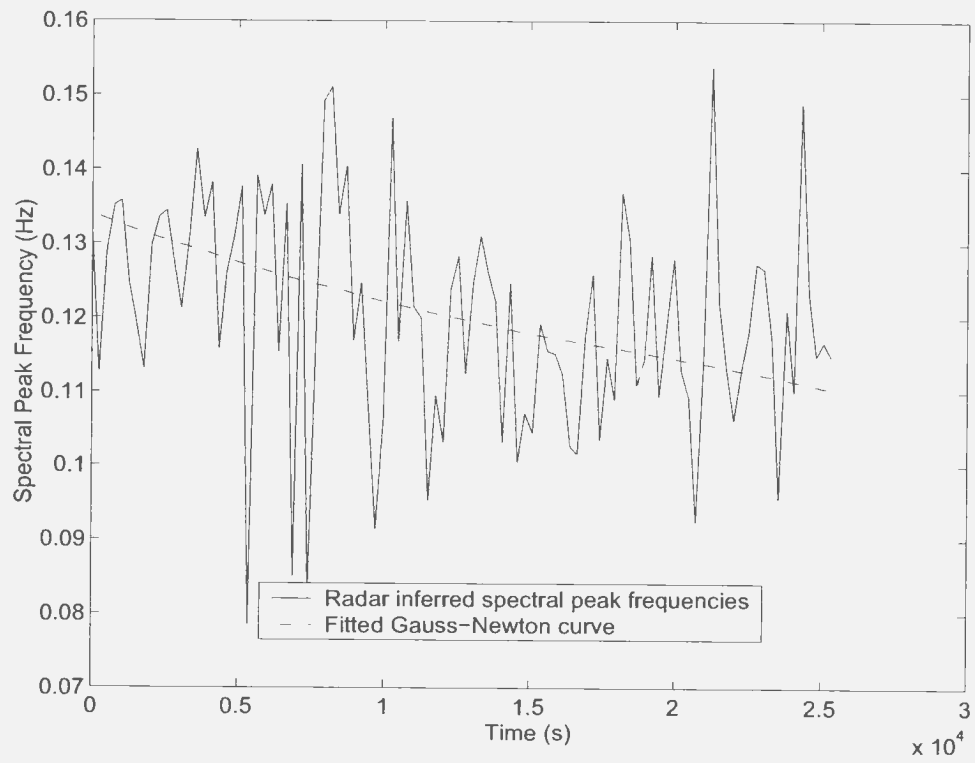


Figure 6.4: Radar-inferred spectral peaks.

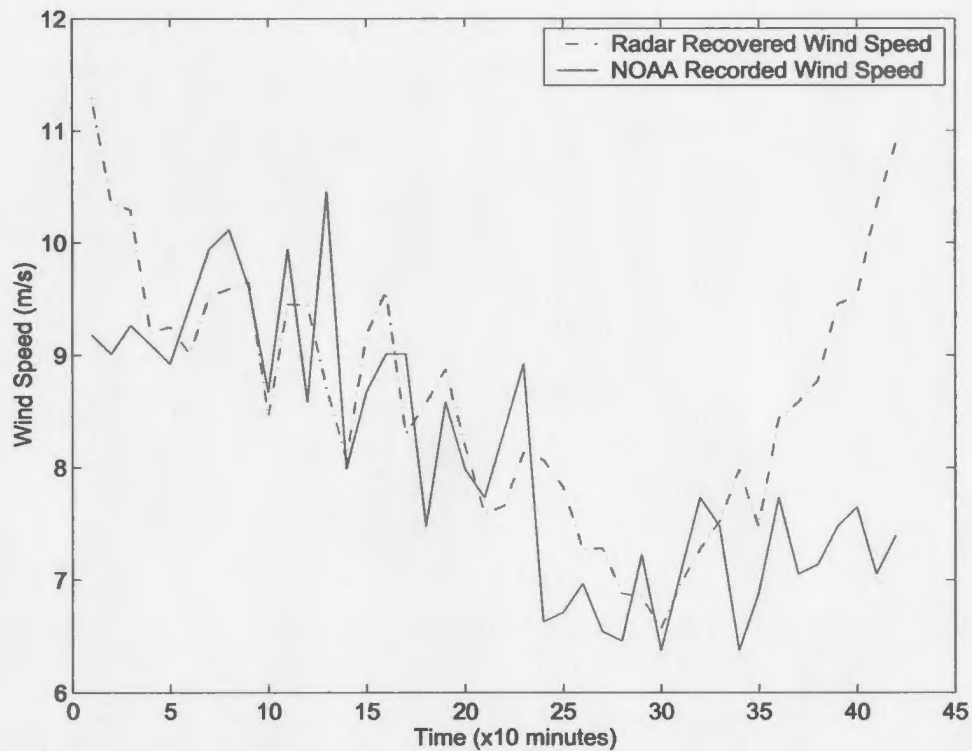


Figure 6.5: Radar recovered and NOAA measured wind speeds.

ground truth values given from the NOAA data. The anemometer employed by the NOAA weather station was situated 29.0 metres above sea level. Hence the values have been adjusted to the standard JONSWAP 10 metre level, using the logarithmic profile of wind speed over the ocean surface.

As can be seen, the radar inferred values closely match the ground truth values. Figure 6.6 shows a percentage error plot for each of the time points. There is a maximum error of 20% throughout, except for the last several points, for which the deviation seems to be greater. This phenomenon is consistent with that observed in Section 5.2 when the same method was applied to simulated noisy data, and is explained in that section.

Figure 6.7 shows the radar recovered wind speed when the numerical spectral growth curve in Section 4.2 was used in the model. The radar-inferred wind speed

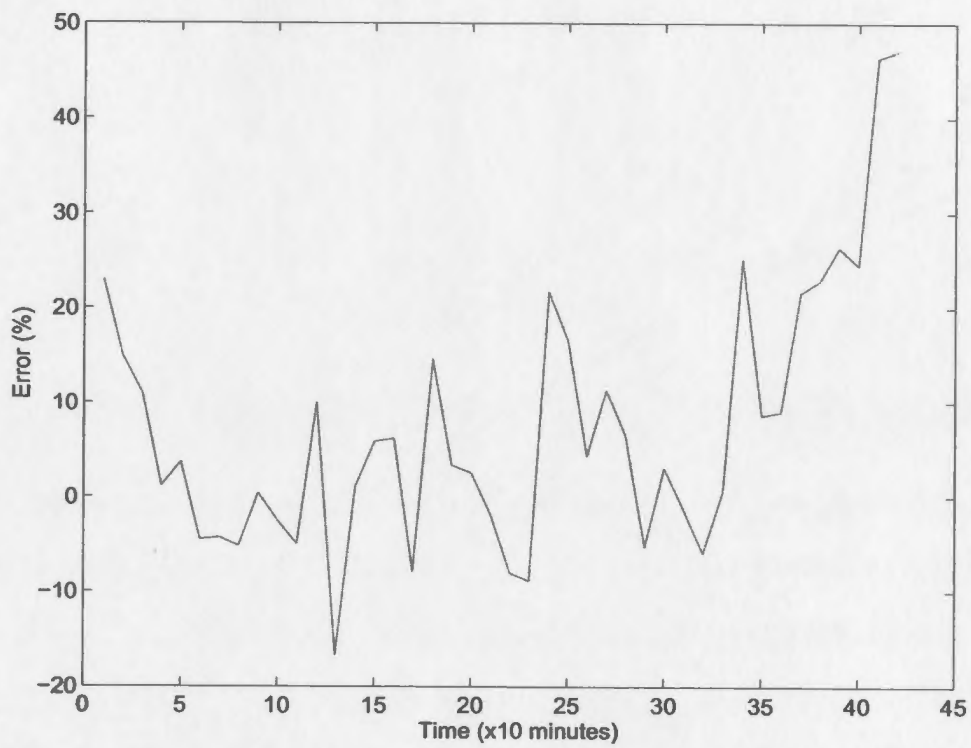


Figure 6.6: Error in radar-inferred wind speed values.

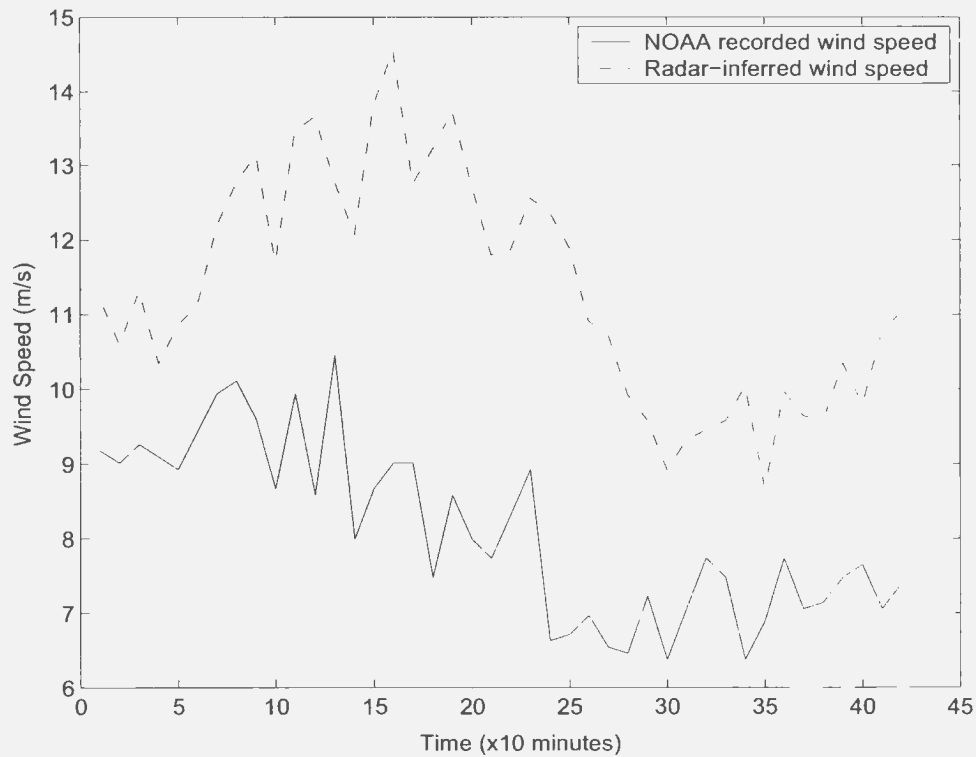


Figure 6.7: Radar recovered values using techniques in Section 4.2.

seems to follow the trend rather faithfully. However, the recovered wind speeds seem to be off by a constant factor of about 30 %. This is quite possibly due to the choice of the  $S_{in}$  term, recalling from Section 4.2 that there are many such models available. Also, it is noted that there is significant computation time required to fit this model using a Gauss Newton algorithm.

## Chapter 7

# Conclusions and Recommendations

In Chapter 3, an expression was derived that related the saturated wind speed to the position of the second order radar cross section peaks along the Doppler axis. This was done by differentiating the mathematical model based on certain assumptions that could be made in the regions of interest. Using the resulting expression, it was possible to extract the saturated wind speed from simulated, ideal radar cross sections to a very high degree of accuracy.

From the radar-inferred saturated wind speed it is possible to calculate the peak frequency of the ocean spectrum. The dependence of ocean spectral growth with respect to both time and local wind conditions was addressed in Chapter 4. A differential equation was derived based on existing JONSWAP models that related wind speed, time, and the spectral peak frequency. By solving this equation using a discrete approximation, it is possible to extract a wind speed record from a time series of ocean spectral peaks. It is also possible to recover the wind speed from spectral peaks using numerical spectrum growth techniques such as the SWAMP project. However, it was found that this method is much more computationally demanding.

The models developed in Chapters 3 and 4 are quite vulnerable to noise. Signal processing techniques were discussed in Chapter 5 that would mitigate the effects of ordinary HF radar noise. These techniques and the models themselves were tested

against simulated noisy data. Finally, in Chapter 6, these methods were applied to real HF radar data obtained by Rutgers University from a CODAR unit operating over the ocean surface near Breezy Point, NY. The wind speeds extracted from the radar data were compared to ground truth data acquired from a weather station operated by NOAA. The results were very encouraging, with an error of less than 20% for the majority of the time series.

## 7.1 Suggestions for Further Work

More Doppler spectra of the HF ocean echo could be obtained and averaged to yield more accurate saturated wind speed values and hence more accurate spectral peak frequency readings. In addition, more spectral peak frequency readings could be obtained over the same period of time – that is, readings could be taken closer than 256 seconds apart. This would result in a better curve fit for the method outlined in Section 5.2.

Note that all of the spectral peak frequency time series was used in the wind speed recovery algorithm. Also the last few wind speed points that were recovered were quite deviant as compared to the rest of the time series. With this in mind, and using the outlined methods, future spectral peak readings are required to obtain an accurate current wind speed reading. A higher density of spectral peak readings would help to lessen this problem, as well as to improve the accuracy. Also, more research could be conducted to develop more sophisticated signal processing techniques than those mentioned in Chapter 5 to yield more accurate results.

More research needs to be conducted on *decaying* sea states. The spectral peak frequency of the illuminated patch of ocean cannot keep decreasing. Eventually, the swell will move out of the fetch region and result in lower or less developed ocean state. The models presented in Chapter 4 do not address an increase in the spectral

peak frequency, though this obviously must happen at some point. The literature appears to be quite scarce on the nature of decaying sea states. This subject needs to be studied further before the presented models can be expanded to incorporate them.

## References

- [1] D. D. Crombie, "Doppler spectrum of sea echo at 13.56 Mc./s," *Nature*, vol. 175, pp. 681-682, April 1955.
- [2] L. Tsang, J. A. Kong, and K. H. Ding, *Scattering of electromagnetic waves. Theories and applications*. Wiley Series in Remote Sensing, Toronto: J. Wiley, 2000.
- [3] D. E. Barrick and W. H. Peake, "A review of scattering from surfaces with different roughness scales," *Radio Science*, vol. 3, pp. 865-868, 1968.
- [4] S. O. Rice, "Reflection of electromagnetic waves from slightly rough surfaces," in *Theory of Electromagnetic Waves* (M. Kline, ed.), pp. 351-378, New York: Interscience, 1951.
- [5] J. R. Wait, "Theory of HF ground wave backscatter from sea waves," *J. Geophys. Res.*, vol. 71, pp. 4839-4842, 1966.
- [6] D. E. Barrick, "Theory of HF/VHF propagation across the rough sea," *Radio Science*, vol. 6, pp. 517-533, 1971.
- [7] J. Walsh, R. Howell, and B. Dawe, "Model development for evaluation studies of ground wave radar." Contract report for the Department of National Defence, Government of Canada, DSS Contract Number W7714-8-5655/01-SS, C-CORE Contract Number 90-C14, 1990.

- [8] J. F. Ward, "Power spectra from ocean movements measured remotely by ionospheric radio backscatter," *Nature*, no. 223, pp. 1325–1330, 1969.
- [9] K. Hasselmann, "Determination of ocean wave spectra from doppler radio return from the sea surface," *Nature Physical Science*, vol. 229, pp. 16–17, 1971.
- [10] D. D. Crombie, "Backscatter of HF radio waves from the sea," in *Electromagnetic Probing in Geophysics* (J. R. Wait, ed.), pp. 131–162, Boulder, Colorado: The Golem Press, 1971.
- [11] D. E. Barrick, "Dependence of second-order sidebands in HF sea echo upon sea state," in *1971 G-AP International Symposium Digest*, (Los Angeles, CA), pp. 194–197, 1971.
- [12] D. E. Barrick, "Remote sensing of sea state by radar," in *Remote Sensing of the Troposphere* (V. E. Derr, ed.), pp. 12–1 – 12–46, Boulder, Colo.: NOAA/Environmental Research Laboratories, 1972.
- [13] E. W. Gill and J. Walsh, "High-frequency bistatic cross sections of the ocean surface," *Radio Science*, vol. 36, pp. 1459–1475, November/December 2001.
- [14] R. H. Stewart and J. R. Barnum, "Radio measurements of oceanic winds at long ranges: An evaluation," *Radio Sci.*, vol. 10, no. 10, pp. 853–857, 1975.
- [15] A. E. Long and D. B. Trizna, "Mapping of North Atlantic winds by HF radar sea scatter interpretation," in *IEEE Transactions on Antennas and Propagation*, vol. 21, pp. 680–685, 1977.
- [16] P. E. Dexter and S. Theodorides, "Surface wind speed extraction from HF sky-wave radar Doppler spectra," *Radio Science*, vol. 17, no. 3, pp. 643–652, 1982.
- [17] M. L. Heron and R. J. Rose, "On the application of HF ocean radar to the

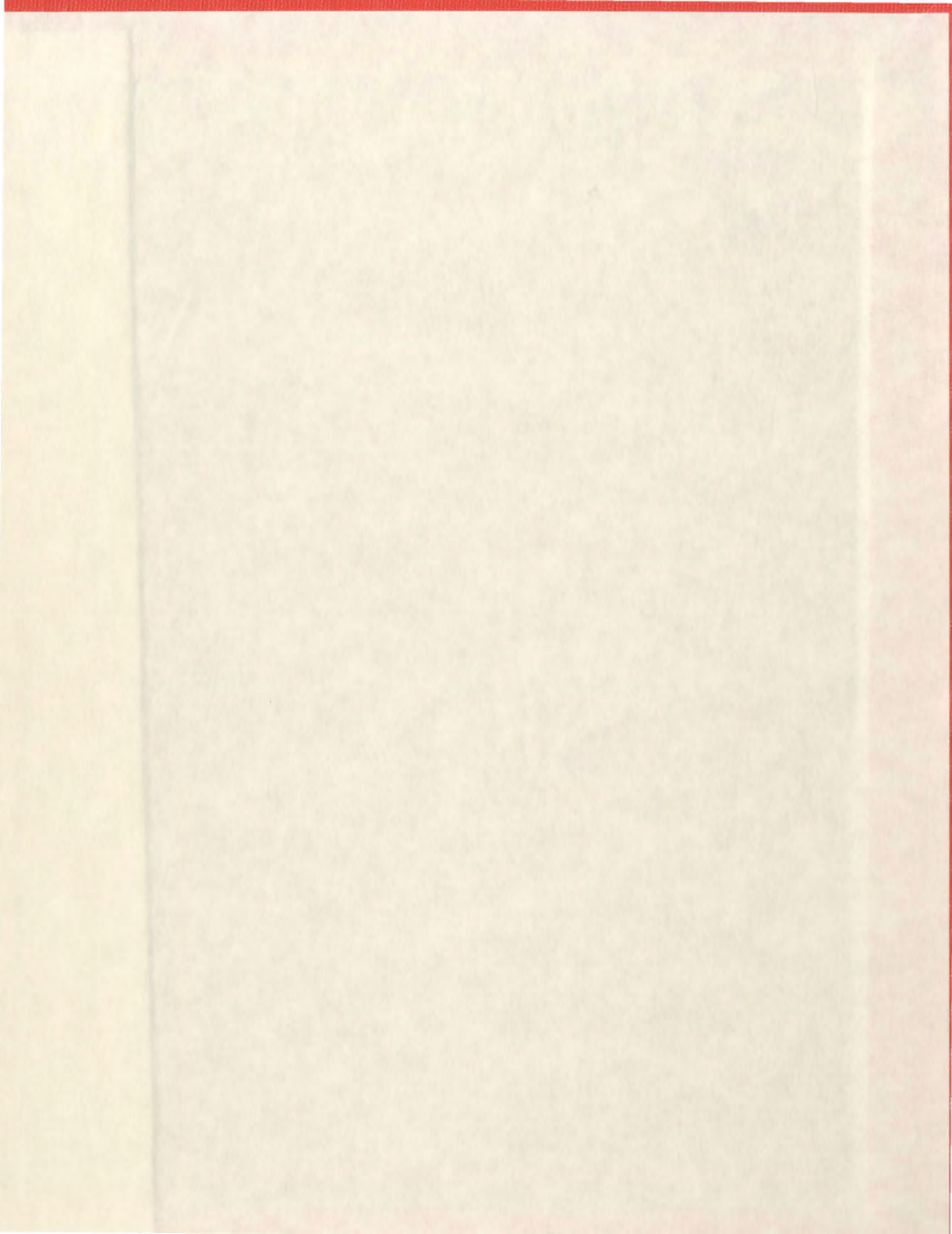
- observation of temporal and spatial changes in wind direction,” *IEEE Journal of Oceanic Engineering*, vol. 11, pp. 210–218, 1986.
- [18] J. W. Maresca and J. R. Barnum, “Estimating wind speed from HF skywave radar sea backscatter,” in *IEEE Transactions on Antennas and Propagation*, vol. AP-30, pp. 846–852, 1982.
- [19] E. W. Gill, *The Scattering of High Frequency Electromagnetic Radiation from the Ocean Surface: An Analysis Based on a Bistatic Ground Wave Radar Configuration*. PhD thesis, Memorial University of Newfoundland, St. John’s, Newfoundland, January 1999.
- [20] D. E. Barrick, J. M. Headrick, R. W. Bogle, and D. D. Crombie, “Sea backscatter at HF: Interpretation and utilisation of the echo,” in *Proc. IEEE*, vol. 62, pp. 673–680, 1974.
- [21] J. L. Ahearn, S. R. Curley, J. M. Headrick, and D. B. Trizna, “Tests of remote skywave measurement of ocean surface conditions.” in *Proceedings of the IEEE*, vol. 62, pp. 681–687, 1974.
- [22] C. Gaffard and J. Parent, “Remote sensing of wind speed at sea surface level using HF skywave echoes from decametric waves,” *Geophysical Research Letters*, vol. 17, no. 5, pp. 615–618, 1990.
- [23] B. Kinsman, *Wind Waves*. Prentice Hall, 1965.
- [24] K. Hasselmann, D. B. Ross, P. Muller, and W. Sell, “A parametric wave prediction model.” *Journal of Physical Oceanography*, vol. 6, pp. 200–228, 1976.
- [25] W. Huang, S. Wu, E. W. Gill, B. Wen, and J. Hou, “HF radar wind and wave measurement over the Eastern China sea,” *IEEE Transactions on Geoscience and Remote Sensing*, vol. 40, September 2002.

- [26] L. R. Wyatt, "High order nonlinearities in HF radar backscatter from the ocean surface," in *IEE proceedings Radar, Sonar, and Navigation*, vol. 142, pp. 293–300, 1995.
- [27] L. R. Wyatt, "HF radar measurements in high sea-states," in *Proceedings of Oceans98*, (Nice, France), IEEE, September 1998.
- [28] L. R. Wyatt, "HF radar wind measurement during NURWEC2," in *Proceedings of IGARSS 88 Symposium*, (Edinburgh), pp. 781–782, 1988.
- [29] F. E. Isaac and L. R. Wyatt, "Segmentation of HF radar measured directional wave spectra using the Voronoi Diagram," *Journal of Atmospheric and Oceanic Technology*, vol. 14, pp. 950–959, 1997.
- [30] U. S. Army Coastal Engineering Research Center, *Shore Protection Manual*. Washington, DC: U. S. Government Printing Office, 1977.
- [31] The SWAMP Group, *Ocean Wave Modelling*. New York: Plenum Press, 1985.
- [32] S. Hasselmann, K. Hasselmann, J. H. Allender, and T. P. Barnett, "Computations and parameterisations of the nonlinear energy transfer in a gravity wave spectrum. part 2: Parameterisations of the nonlinear energy transfer for application in wave models.," *Journal of Physical Oceanography*, vol. 15, pp. 1378–1391, 1985.
- [33] D. Resio and W. Perrie. "A numerical study of non-linear energy fluxes due to wave-wave interactions. part 1: Methodology and basic results," *Journal of Fluid Mechanics*, vol. 223, pp. 609–629, 1991.
- [34] H. Charnock, "Wind stress over a water surface," *Quarterly Journal of the Royal Meteorological Society*, vol. 81, pp. 639–640, 1955.

- [35] B. J. Lipa and D. E. Barrick, "Analysis methods for narrow-beam high-frequency radar sea echo," tech. rep., National Oceanic and Atmospheric Administration, 1982.
- [36] S. C. Chapra and R. P. Canale, *Numerical Methods for Engineers*. Toronto: McGraw-Hill, 3rd ed., 1998.
- [37] B. Dawe, "Radio wave propagation over earth: Field calculations and an implementation of the roughness effect," Master's thesis, Memorial University of Newfoundland, St. John's, Newfoundland, 1988.
- [38] International Telecommunications Union, "Propagation in ionized media," in *ITU-R Recommendations, 1994 PI Series Volume*, (Geneva), 1994.
- [39] W. Pierson, "Wind generated gravity waves," *Advances in Geophysics*, vol. 2, pp. 93-178, 1955.
- [40] G. J. Komen, L. Cavaleri, M. Donelan, K. Hasselmann, S. Hasselmann, and P. A. Janssen, *Dynamics and Modelling of Ocean Waves*. Cambridge University Press, 1994.
- [41] K. Hasselmann, "On the non-linear energy transfer in a gravity-wave spectrum, part 1. general theory," *Journal of Fluid Mechanics*, vol. 12, pp. 481-500, 1962.
- [42] U. S. Army Coastal Engineering Research Center, *Shore Protection Manual*. Washington, DC: U. S. Government Printing Office, 1984.
- [43] I. R. Young. *Wind Generated Ocean Waves*, vol. 2 of *Elsevier Ocean Engineering Book Series*. New York: Elsevier, 1999.
- [44] R. E. Walpole, R. H. Myers, and S. L. Myers, *Probability and Statistics*. Prentice Hall, 6th ed., 1998.

- [45] M. Ediger, "A Gauss-Newton method for nonlinear regression," *The Mathematica Journal*, vol. 1, no. 2, pp. 42–44, 1990.
- [46] B. J. Lipa and D. E. Barrick, "Least-squares methods for the extraction of surface currents from CODAR crossed-loop data: application at ARSLOE," *IEEE Journal of Oceanic Engineering*, vol. 8, pp. 226–253, October 1983.





1911  
1912